HAL
open science

A sedimentary origin for intercrater plains north of the Hellas basin: Implications for climate conditions and erosion rates on early Mars

Francesco Salese, V. Ansan, Nicolas Mangold, John Carter, Anouck Ody, François Poulet, Gian Gabriele Ori

To cite this version:

Francesco Salese, V. Ansan, Nicolas Mangold, John Carter, Anouck Ody, et al.. A sedimentary origin for intercrater plains north of the Hellas basin: Implications for climate conditions and erosion rates on early Mars. Journal of Geophysical Research. Planets, 2016, 121 (11), pp.2239-2267. 10.1002/2016JE005039 . hal-02305998

HAL Id: hal-02305998

https://hal.science/hal-02305998v1

Submitted on 4 Oct 2019

HAL is a multi-disciplinary open access archive for the deposit and dissemination of scientific research documents, whether they are published or not. The documents may come from teaching and research institutions in France or abroad, or from public or private research centers.

L'archive ouverte pluridisciplinaire **HAL**, est destinée au dépôt et à la diffusion de documents scientifiques de niveau recherche, publiés ou non, émanant des établissements d'enseignement et de recherche français ou étrangers, des laboratoires publics ou privés.

AGU PUBLICATIONS

JGR

Journal of Geophysical Research: Planets

RESEARCH ARTICLE

10.1002/2016JE005039

Key Points:

- Intercrater plains on the northern rim of Hellas basin are composed of Noachian sedimentary rocks locally overlain by Hesperian volcanic rocks
- Sedimentary rocks are composed predominantly of subhorizontal planar layers and fill depressions such as old craters
- Sedimentary rocks were eroded at a rate of ~1000 nm yr−1 before the volcanic flows emplaced 3.3 Ga ago

Correspondence to:
F. Salese,
francesco.salese@unich.it

Citation:
Salese, F., V. Ansan, N. Mangold, J. Carter, A. Ody, F. Poulet, and G. G. Ori (2016), A sedimentary origin for intercrater plains north of the Hellas basin: Implications for climate conditions and erosion rates on early Mars, *J. Geophys. Res. Planets*, *121*, 2239–2267, doi:10.1002/2016JE005039.

Received 22 MAR 2016
Accepted 30 SEP 2016
Accepted article online 7 OCT 2016
Published online 14 NOV 2016

©2016. American Geophysical Union. All Rights Reserved.

A sedimentary origin for intercrater plains north of the Hellas basin: Implications for climate conditions and erosion rates on early Mars

Francesco Salese[1,2], Veronique Ansan[2], Nicolas Mangold[2], John Carter[3], Anouck Ody[4], Francois Poulet[3], and Gian Gabriele Ori[1,5]

[1]International Research School of Planetary Sciences, Dipartimento di Ingegneria e Geologia, Università Gabriele D'Annunzio, Pescara, Italy, [2]Laboratoire de Planétologie et de Géodynamique de Nantes, UMR6112, CNRS/Nantes University, Nantes, France, [3]Institut d'Astrophysique Spatiale, Université Paris Sud 11, Orsay, France, [4]Laboratoire de Géologie de Lyon: Terre, Planètes, Environnement, Université de Lyon 1 (CNRS, ENS-Lyon, Université de Lyon), Villeurbanne, France, [5]Ibn Battuta Centre, Université Cady Ayyad, Marrakesh, Morocco

Abstract Understanding the origin (volcanic or sedimentary) and timing of intercrater plains is crucial for deciphering the geological evolution of Mars. We have produced a detailed geological map of the intercrater plains north of the Hellas basin, based on images from the Mars Express High-Resolution Stereo Camera, the Mars Reconnaissance High-Resolution Imaging Science Experiment, and Context. Erosional windows and fresh impact craters provide a way of studying the lithology of intercrater plain units. They are composed predominantly of light-toned sedimentary rocks with subhorizontal bedding over a broad extent (greater than tens of kilometers), showing cross-bedding stratifications locally. The broad extent, geometry, and flat topography of these sediments favor a formation by aqueous processes (alluvial and lacustrine) rather than airfall (eolian and volcaniclastic). The Late Noachian (~3.7 Ga) sedimentary plains are locally covered by dark-toned, rough-textured lava flows of Late Hesperian age (~3.3 Ga). Fe/Mg phyllosilicates were detected within sedimentary rocks, whereas volcanic rocks contain pyroxene and lack signatures of alteration, in agreement with interpretations made from texture and morphology. In erosional windows, the superimposition of sedimentary rocks by younger volcanic flows enables the estimation of an erosion rate of ~1000 nm yr^{-1} during the Hesperian period (3.3–3.7 Ga). Thus, our study shows that an intense sedimentary cycle occurred on the northern rim of the Hellas basin before and during the Late Noachian, leading to the formation of widespread sedimentary plains, which were then eroded, in agreement with a gradual change in the climatic conditions in this period, and later covered by volcanic flows.

1. Introduction

The heavily cratered Martian highlands, dated to >3.7 Gy [*Tanaka*, 1986; *Hartmann and Neukum*, 2001; *Hartmann*, 2005], exhibit smooth surfaces between impact craters typically larger than 50 km in diameter [*Malin*, 1976]. Such surfaces were named "intercrater plains." Their origin is a major unresolved issue, despite the fact that several works have focused on their surface properties or composition [*Malin*, 1976; *Malin and Dzurisin*, 1977; *Greeley and Spudis*, 1981; *Tanaka and Davis*, 1988; *Edgett and Malin*, 2002; *Rogers et al.*, 2009; *Rogers and Fergason*, 2011; *Ody et al.*, 2013; *Rogers and Nazarian*, 2013; *Edwards et al.*, 2014]. Intercrater plains were interpreted as being formed by either volcanic flows, sedimentary rocks, or impact breccias, or a combination of these lithologies [*Malin*, 1976; *Tanaka and Davis*, 1988]. Volcanic materials were initially favored because smooth plains show the same characteristics as those of volcanic lunar mare, i.e., lava flow fronts and local vents [*Wilhelms*, 1974; *Malin*, 1976; *Tanaka and Davis*, 1988]. Later, this interpretation was locally confirmed by the presence of mafic minerals such as olivine and pyroxene detected by orbital spectrometers [*Christensen et al.*, 1998; *Bandfield et al.*, 2000; *Bandfield*, 2002; *Bandfield and Smith*, 2003; *Christensen et al.*, 2003; *Hoefen et al.*, 2003; *Christensen et al.*, 2004; *Hamilton and Christensen*, 2005; *Bibring et al.*, 2006; *Murchie et al.*, 2007; *Poulet et al.*, 2007; *Mustard et al.*, 2008; *Poulet et al.*, 2009a, 2009b; *Carter et al.*, 2013a; *Ody et al.*, 2013]. However, to date, the presence of volcanic plains has not precluded the existence of sedimentary rocks, especially on ancient plains coeval with the fluvial erosion of the highlands [*De Hon*, 1992; *Ori et al.*, 2000; *Moore and Howard*, 2005; *Mangold and Ansan*, 2006; *Pondrelli et al.*, 2008; *Metz et al.*, 2009; *Di Achille and Hynek*, 2010].

Although several studies have focused on the lithology of these intercrater plains, recent missions revealed several characteristics favoring a sedimentary origin for some of them, including the presence of fluvial landforms or light-toned layers locally displaying hydrated minerals [*Craddock and Maxwell*, 1993; *Craddock et al*., 1997; *Moore and Howard*, 2005; *Mangold and Ansan*, 2006; *Milliken et al*., 2007; *Murchie et al*., 2007; *Ehlmann et al*., 2008; *Mustard et al*., 2008; *Pondrelli et al*., 2008; *Loizeau et al*., 2012; *Carter et al*., 2013a]. Identifying the lithology of intercrater plains is challenging owing to the difficulty in discriminating between volcanic flows and sedimentary rocks within heavily cratered surfaces. However, whether these plains are constituted of volcanic or sedimentary rocks is fundamentally different when trying to constrain their formation processes and environmental conditions. When plains are formed by sedimentary deposition, knowing their lithology is especially important because their formation can be linked to aqueous processes and past climate evolution. Intercrater plains, recording geologic and bombardment history, are of fundamental importance in understanding the internal and external evolution of planetary bodies [*Leake*, 1982].

Our study focuses on the northern rim of the Hellas basin (Figure 1a), extending from 291°W to 309°W and 17°S to 31°S (Figure 1b), where many intercrater plains are present. This region of the Hellas basin is of particular geological interest because it shows a relatively flat area (Figure 1b), compared to the other areas of the Hellas rim, standing between −1 km and 0 km and covering a WNW-ESE trending area of about 170,000 km^2. Intercrater plains were previously mapped as Noachian/Hesperian undifferentiated material units, thus of unknown lithology [*Tanaka*, 1986; *Leonard and Tanaka*, 2001; *Tanaka et al*., 2014]. To determine the origin of intercrater plains and their lithology, we produced a geological map at the 1:25,000 scale, using multiple data sets including altimetry, visible images at various spatial resolutions (e.g., from 50 m pixel^{-1} to 25 cm pixel^{-1}), and thermal infrared images at 100 m pixel^{-1}. The proposed geological map takes into account both the analysis of landforms and geological features (hills, plains, fresh impact craters, lava flows, layers, etc.), and the age of each unit identified by crater counts. Our geological map is then correlated to mineralogical maps from near-infrared spectrometers for further determination of the lithology. The discussion focuses on the implications of these observations on the Noachian and Hesperian evolution of North Hellas.

2. Geological Setting and Previous Mapping

The Hellas basin (270°–316°W/20°–58°S), formed by a large impact event, consists of an elliptical impact crater with a minor axis of ~5000 km and a major axis of ~6000 km (taking the rim into account). After its formation ~4.0 Ga years ago [*Werner*, 2008], the Hellas basin played the role of depositional sink and was partly surrounded by Hesperian volcanic provinces (e.g., Hadriaca Patera and Tyrrhena Patera) [*Williams et al*., 2009]. Based on the Mars Orbiter Laser Altimeter (MOLA) topography [*Smith et al*., 1999], the northwestern shoulder of the Hellas basin shows a relatively flat region (between −1 km and 0 km, approximately) distinct from otherwise gently sloping areas toward the basin center (Figure 1b). This northwestern Hellas rim is characterized by hilly, cratered highlands with smooth intercrater plains. Figure 1b displays this relatively flat area which contains large, degraded impact craters (>50 km in diameter).

Mapping of the Hellas region was attempted from Mariner 9 [*Potter*, 1976; *Scott and Carr*, 1978] and Viking data at the 1:15,000,000 scale [*Greeley and Guest*, 1987; *Tanaka et al*., 2014], while other studies of the Hellas basin updated the mapping of the entire region at the 1:5,000,000 scale [*Tanaka and Leonard*, 1995; *Leonard and Tanaka*, 2001] or more in detail [*Moore and Wilhelms*, 2007]. They mapped the oldest rocks, locally present in our studied area, as Early Noachian heavily cratered materials [*Tanaka*, 1986; *Leonard and Tanaka*, 2001; *Werner*, 2008]. Note that the recent global map by *Tanaka et al*. [2014] was made at a smaller scale (1:20,000,000) and cannot provide all the details needed to identify individual intercrater plains.

Figure 2 shows the principal units mapped by *Leonard and Tanaka* [2001] at a scale of 1:4,336,000, i.e., 200 times smaller than our scale (1:25,000). The Nm and Nh units represent the Noachian basement rocks uplifted during the Hellas impact. The Npld and Npl2 units correspond to highly cratered and intercrater plain material (see *Leonard and Tanaka* [2001] for more details). The Nh1 unit consists of Noachian etched material of degraded plains, interpreted by *Leonard and Tanaka* [2001] as sedimentary in origin. The Hplm unit represents Hesperian volcanic deposits filling the smooth plains. The latter unit (Hplm) is mapped as being present in our study area north of the Niesten crater (302.3°W/28.3°S). In these previous works, the intercrater plains, easily discernible on the topographic map (Figure 1b), were not individually mapped and their lithology remained undefined. In addition, east of our study area, possible sedimentary rocks were mapped, labeled

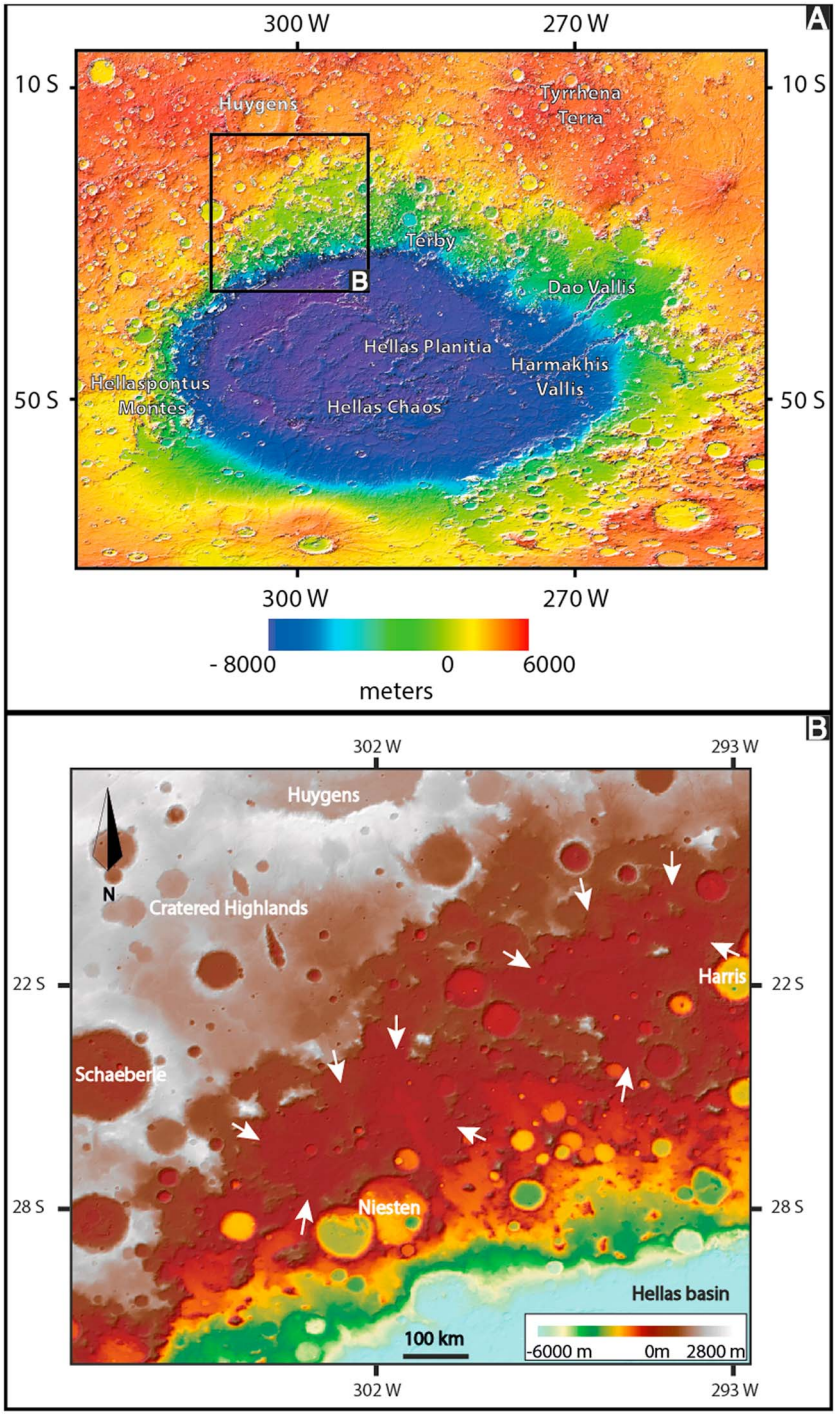

Figure 1. (a) MOLA topographic map centered on the Hellas impact basin, showing our studied area located on its northwestern rim (black box). (b) MOLA topographic map centered on the NW rim of the Hellas basin, showing the basin (blue) in the lower right corner, the cratered highlands (grey-white) in the upper left corner and a relatively flat area (red) limited by white arrows, standing between −1 km and 0 km, and covering a WNW-ESE trending area of ~170,000 km^2.

HNe, such as those inside the Schaeberle, Terby, and Millochau craters, which were confirmed as sedimentary by recent data [*Crown et al.*, 2005; *Ansan et al.*, 2011].

Given the amount of new data, a new mapping campaign was required to enable a better assessment of the nature of the various units in this complex area and to provide bases for further interpretations of their origin

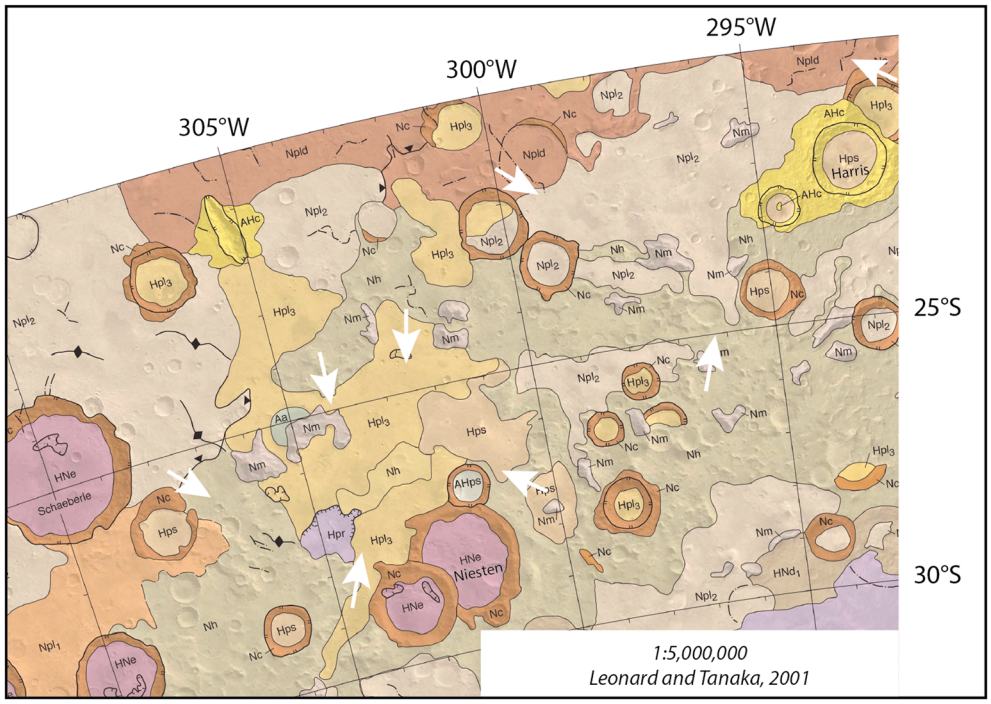

Figure 2. Extract of the geological map of *Leonard and Tanaka* [2001]. The map has the same extent as the MOLA shaded relief in Figure 1b. The massif unit (Nm) consists of large, isolated, resistant blocks of the Noachian period while the hilly unit (Nh) is relatively less rugged and includes uplifted material, basin ejecta, and younger, undifferentiated mantling deposits of uncertain origin. The outer rim of the Hellas basin is embayed by the Middle Noachian cratered (unit Npl_1), Middle Noachian dissected (unit Npld), and Upper Noachian subdued cratered (unit Npl_2) units of the plateau sequence. The smooth Hesperian unit (Hpl_3) of the plateau sequence probably includes volcanic, eolian, and fluvial deposits, which partly bury low areas and crater floors on the Hellas basin rim. The Hps unit forms the older smooth plain material, locally fills impact craters and embays and partly buries older highland and Hellas rim units. Unit HNe consists of degraded plain deposits of varying thickness scattered about on the Hellas basin rim. White arrows indicate the location of the relatively flat area shown in Figure 1b.

(s). Our mapping, described in section 4, is consistent with previous mapping at a regional scale but shows marked differences in individually mapped intercrater plains, which are the focus of this study.

3. Data and Geological Mapping Process

3.1. Data

Visible imagery at different scales, in association with thermal imagery, was used to discriminate geological units. Thermal Emission Imaging System (THEMIS) nighttime images [*Christensen et al.*, 2004] were used to discriminate qualitatively the degree of induration/compaction from which the relative grain size can be deduced at a spatial sampling of 100 m pixel^{-1}. A mosaic of High-Resolution Stereoscopic Camera (HRSC) nadir images [*Neukum and Jaumann*, 2004; *Jaumann et al.*, 2007] was used for morphological interpretations at a regional scale at a spatial sampling of ~12.5 m pixel^{-1} at best. The Context (CTX) camera (average image scale of 6 m pixel^{-1}) [*Malin et al.*, 2007] and the High-Resolution Imaging Science Experiment (HiRISE) camera (image scale of 25 cm pixel^{-1}) [*McEwen et al.*, 2007] provided detailed images, useful for identifying layering and surface texture.

Imagery was used in association with altimetry data at different scales, such as that from the Mars Orbiter Laser Altimeter (MOLA) [*Smith et al.*, 1999] at ~463 m pixel^{-1} of gridding, digital elevation models (DEMs) constructed from HRSC stereo images at ~50–150 m pixel^{-1} of gridding, and CTX and HiRISE DEMs (with gridding of 6 m pixel^{-1} and 1 m pixel^{-1}, respectively) processed from stereo pairs through the NASA Ames Stereo Pipeline (m pixel^{-1}) [*Broxton and Edwards*, 2008; *Moratto et al.*, 2010]. The HRSC DEM and images cover almost the whole of the study area, and the CTX DEM and images cover about 80% while the HiRISE DEM and images cover about 2% of the study area and were used for detailed observations only.

Lastly, data from the Observatoire pour la Minéralogie, l'Eau, les Glaces et l'Activité (OMEGA) [*Bibring et al*., 2004] and the Compact Reconnaissance Imaging Spectrometer for Mars (CRISM) [*Murchie et al*., 2007] were used for mineralogical analysis of some of the different units identified from visible images after the mapping was achieved.

3.2. Geological Mapping

All data were integrated into the ArcGIS software package version 10.2.2 using equirectangular map projection. Units were identified by (i) their main topographic and geological characteristics (e.g., hill, plain, impact crater, and ejecta), (ii) their surface properties (e.g., rough or smooth surface, including information from relative brightness temperatures in THEMIS images) and (iii) their orbital facies (e.g., layering, bedforms, and cross beddings) defined at the CTX and HiRISE scales into erosional windows, crater walls, or scarps, which enabled their observation in fresh sections.

Our mapping does not include recent mantling such as recently active dunes or thin ice-rich latitude-dependent mantle (usually shallow enough to be ignored). Geomorphic features were locally superimposed on the map, such as fluvial landforms (valleys and alluvial fans). Our geological map takes into account the relative age from crosscutting relationships. Contacts observed due to crater walls or hills were helpful in elucidating vertical and lateral relationships between mapped units. These stratigraphic relationships were supported by crater-counting methods giving an absolute age (sections 3.3 and 6).

Intercrater plains of the northern Hellas basin were divided into sedimentary and volcanic units, based on the geological properties defined above, as explained in detail in sections 4.2 and 4.3, respectively. To be more specific, these two types of unit were identified as distinct from each other when applying the various criteria above (texture, landforms, geometry, etc.). Volcanic flows, as observed in other regions on Mars, display a rough texture, dark tone and present local vents or dikes typical of effusive flows. In cross section, they can show thick layers (typically >10 m, as observed on the walls of Valles Marineris) but lack thin layering, cross bedding, and lateral continuity. Sedimentary units, as observed in other regions of Mars (e.g., the Terby crater, *Ansan et al*. [2011]), display a smooth surface in planar view, and a complex architecture in section, with thin ($<<10$ m) light-toned layers and local cross bedding. The case of sedimentary plains is developed in the discussion (section 6) to understand further their origin.

3.3. Age Determinations Using Crater-Age Dating

Crater-counting methods were used to estimate the absolute ages of intercrater plain surfaces. Crater counts were performed on Context Camera (CTX; 5–6 m pixel^{-1}) data using Crater Tools [*Kneissl et al*., 2011]. Sinusoidal projection was used for the crater counting and a three-point method to map the craters, at a fixed map scale of 1:18,000. Buried craters (with no or partial rims exposed, often named *ghost craters*) were not included in the crater counts of intercrater plains nor were dense fields of secondary craters. Craters larger than 700 m in diameter were used to fit the isochrons. Below 700 m in diameter, crater counts tend to cross isochrons rather than follow them, showing that erosion or burial has affected craters smaller than this diameter. Crater statistics and crater model ages were analyzed with Craterstats2 software [*Michael and Neukum*, 2010; *Michael et al*., 2012; *Michael*, 2013] using the production function of *Ivanov* [2001] and the chronology *Hartmann and Neukum* [2001].

4. Results

Our geological map (Figure 3a) at the 1:25,000 scale shows the spatial distribution of geological units arranged chronologically. The map spans from 291°E to 309°E and 17°S to 31°S. This part of the northern Hellas rim is bounded to the south by the Hellas basin and to the north by a dense pattern of valley networks. A color classification was used to distinguish the lithology of the material, arranged from older to younger units: brown units correspond to the oldest bedrock, green units to sedimentary rocks, purple units to volcanic rocks, such as lava flows, and yellow units to impact craters and their ejecta. The latter were mapped, using different shades, following the three classes defined from morphology and topography by *Mangold et al*. [2012], see section 4.4. The main geological units are described hereafter according to the chronological order of their formation as deduced from crosscutting relationships and crater counts.

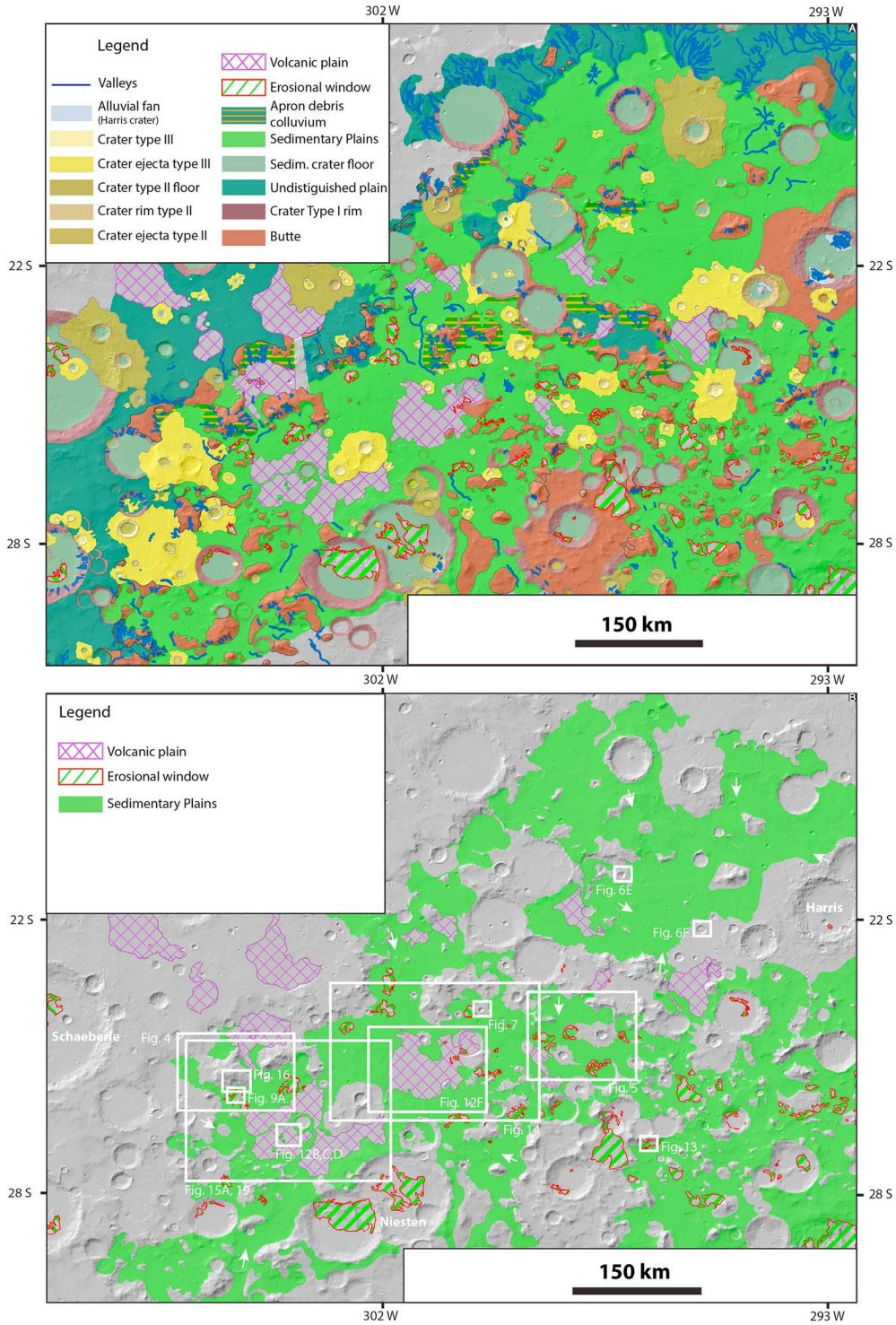

Figure 3. (a) Our geological map of the studied area at the CTX scale. Its extent is about the same as the *Leonard and Tanaka* [2001] map shown in Figure 2. Old rim craters and remnant hills of the basement are mapped in dark and light brown, respectively. Terrains interpreted as sedimentary rocks are mapped with different shades of green: pale green for crater floors; other shades of dark green for units whose origin remains uncertain due to the lack of erosional windows; light green for the sedimentary unit described in detail in the manuscript. Terrains interpreted as volcanic flows are mapped in purple. Different shades of yellow are used to map craters of types II and III (see text) and related ejecta. Morphological features such as valleys and alluvial fans are superimposed. (b) Location of intercrater plains superimposed on the MOLA shaded relief map, whose lithology is identified (sedimentary in green and volcanic in purple) and associated erosional windows (red contour).

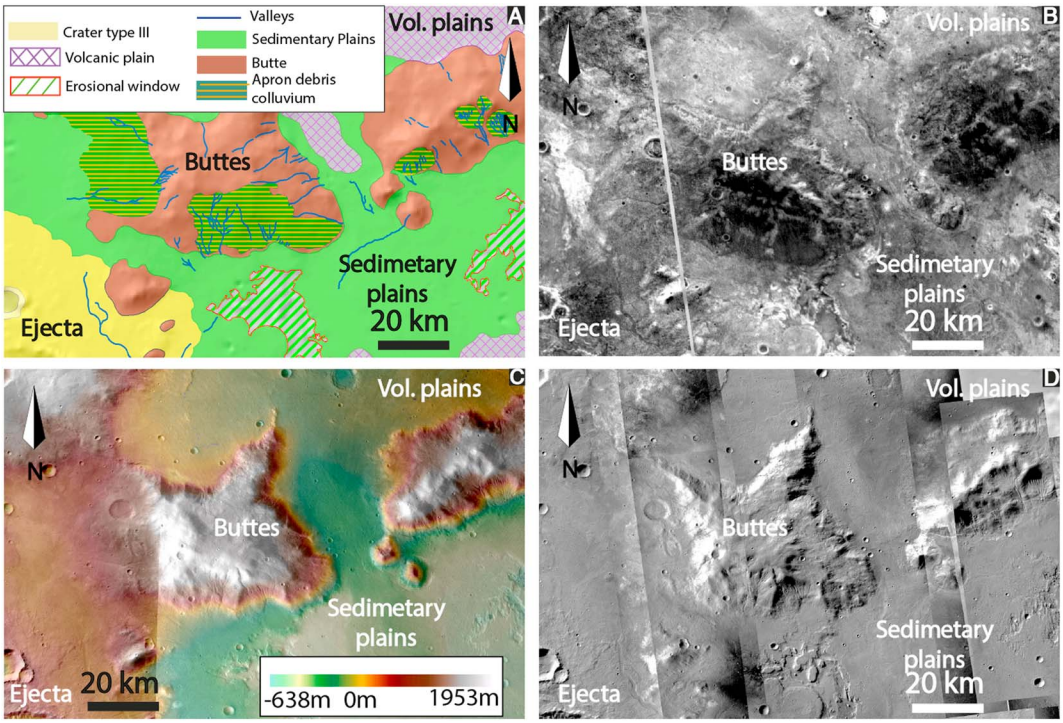

Figure 4. (a) Geological map showing buttes (brown), which are interpreted as crustal bedrock mantled by loose deposits (dark green and orange lines) and carved by some shallow valleys. Color representations are the same as in Figure 3a. (b) Nighttime THEMIS image showing a low brightness temperature on buttes and a medium to high brightness temperature on sedimentary and volcanic plains. (c) HRSC topography showing the two isolated major buttes standing above the smooth plains. (d) CTX images showing the two isolated buttes above smooth plains. CTX images: P22_009640_1543; G15_023947_1535; F01_036052_1543; F04_037252_1545; P12_005711_1546; P22_009785_1544; F02_036474_1549; and D02_027903_1551. See Figure 3b for context.

4.1. Ancient Crustal Bedrock Units

Ancient crustal bedrock is mapped as brown buttes (Figure 3a). They are observed both as rims of degraded impact craters and as hills rising from 2000 to 3000 m above the surrounding plains (Figure 4). The hillslopes are often steep and incised by narrow, poorly branched fluvial valleys. At the HRSC and CTX scales (Figure 4d), these buttes show a relatively smooth surface, suggesting that they are mantled by fine-grained material. This observation is confirmed by the relatively low brightness temperature in nighttime THEMIS images (Figure 4b), implying either the presence of fine-grained loose deposits on the buttes or a poorly indurated and weathered bedrock. This mantling prevents identification of the lithology. Buttes are distributed evenly throughout the study area without any apparent spatial organization (Figure 3a).

We interpret these buttes as inselbergs [*Whittow*, 1984], composed of crustal bedrock whose lithology remains unknown, probably old crustal material belonging to the Hellas basin rim. These buttes have undergone a strong erosion and weathering. They are mapped as the oldest geological unit based on relative stratigraphy: smooth plains fill the depressions between hills. This interpretation is similar to earlier ones (Nm unit in *Leonard and Tanaka* [2001]), but only the main buttes were mapped previously; our mapping shows more buttes of a similar nature.

4.2. Sedimentary Units

Terrains interpreted as sedimentary rocks are mapped in green (Figures 3 and 5). They show the same general characteristics, such as intermediate to high brightness in visible imagery, a relatively smooth surface at the HRSC and CTX imagery scales, a layered internal structure at the HiRISE imagery scale, and a low to intermediate brightness temperature in nighttime THEMIS. The distribution of the sedimentary units is very homogeneous, covering a surface area of about 320,000,000 km^2, spanning 291°E to 309°E and 17°S to 31°S. Furthermore, sedimentary units are restricted to elevations between +500 m and −2000 m.

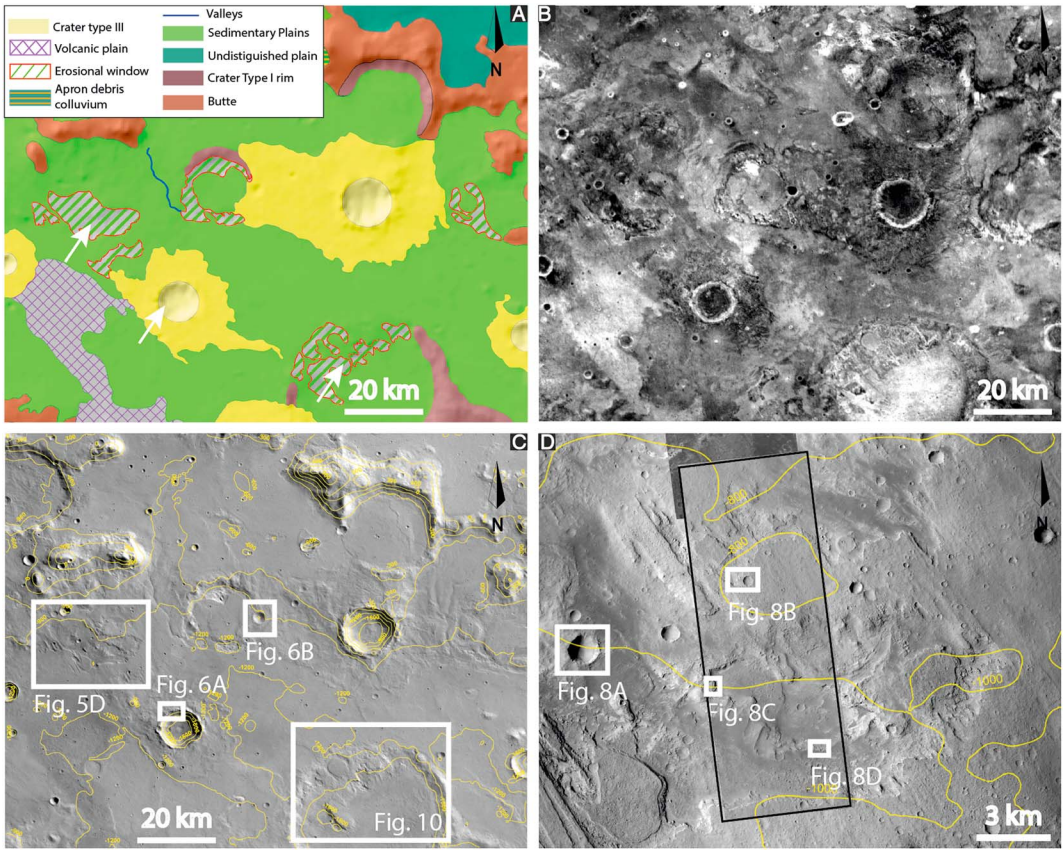

Figure 5. (a) Geological map showing smooth plains (light green), consisting of sedimentary rocks whose geometrical structure is visible in erosional windows and fresh crater rims (as indicated by the white arrows in the figure). Color representations are the same as in Figure 3a. (b) Nighttime THEMIS image showing medium to high thermal brightness terrains associated with the sedimentary rocks. Volcanic flows are also characterized by high or very high thermal brightness. (c) HRSC image showing smooth plains, impact craters, ghost craters, and isolated buttes on which HRSC topographic contour lines are superimposed with a relief interval of 300 m. (d) CTX (D05_029116_1551) images showing erosional windows within the sedimentary rocks; HiRISE frame ESP_029116_1550 is draped on the CTX images. HRSC topographic contour lines are superimposed with a relief interval of 200 m. See Figure 3b for context.

A key observation to understand the nature of the intercrater plains comes from erosional windows (Figure 5), which enable the reconstruction of the stratigraphy of several smooth plains. There are additional windows from fresh craters excavating these terrains (Figure 6). On Mars, it is rare to find so many erosional windows to investigate the substratum lithology using natural sections. The two major sedimentary units are observed in intercrater plains and large crater floors, which are described in detail below, with minor sedimentary units.

4.2.1. Sedimentary Plains

The sedimentary intercrater plains cover an area of 253,653,000 km^2, spanning 291°E to 309°E and 17°S to 31° S (light green unit, Figure 3a), standing between 0 and −2000 m of elevation (Figure 1b). The surface of the intercrater plains at low to medium resolution (HRSC) is essentially smooth and featureless (Figure 5c).

Going into more detail and mapping at a local scale (1:25,000) using CTX images, large erosional windows and fresh impact craters were found and used as natural geological cross sections to study the stratigraphy of these rocks more closely (Figures 5 to 9). Stratigraphic sections of the layered rocks are observed over thousands of square kilometers in a dozen impact craters (Figures 6 and 7) and in 10 different erosional windows (their location is marked in Figure 3a, see the legend).

First, relatively fresh impact craters <10 km in diameter display numerous natural geological cross sections in sedimentary intercrater plains. All sections show finely layered relatively light-toned material at the CTX and HiRISE scales (Figures 6–8). These layers are relatively subplanar, showing different degrees of induration or

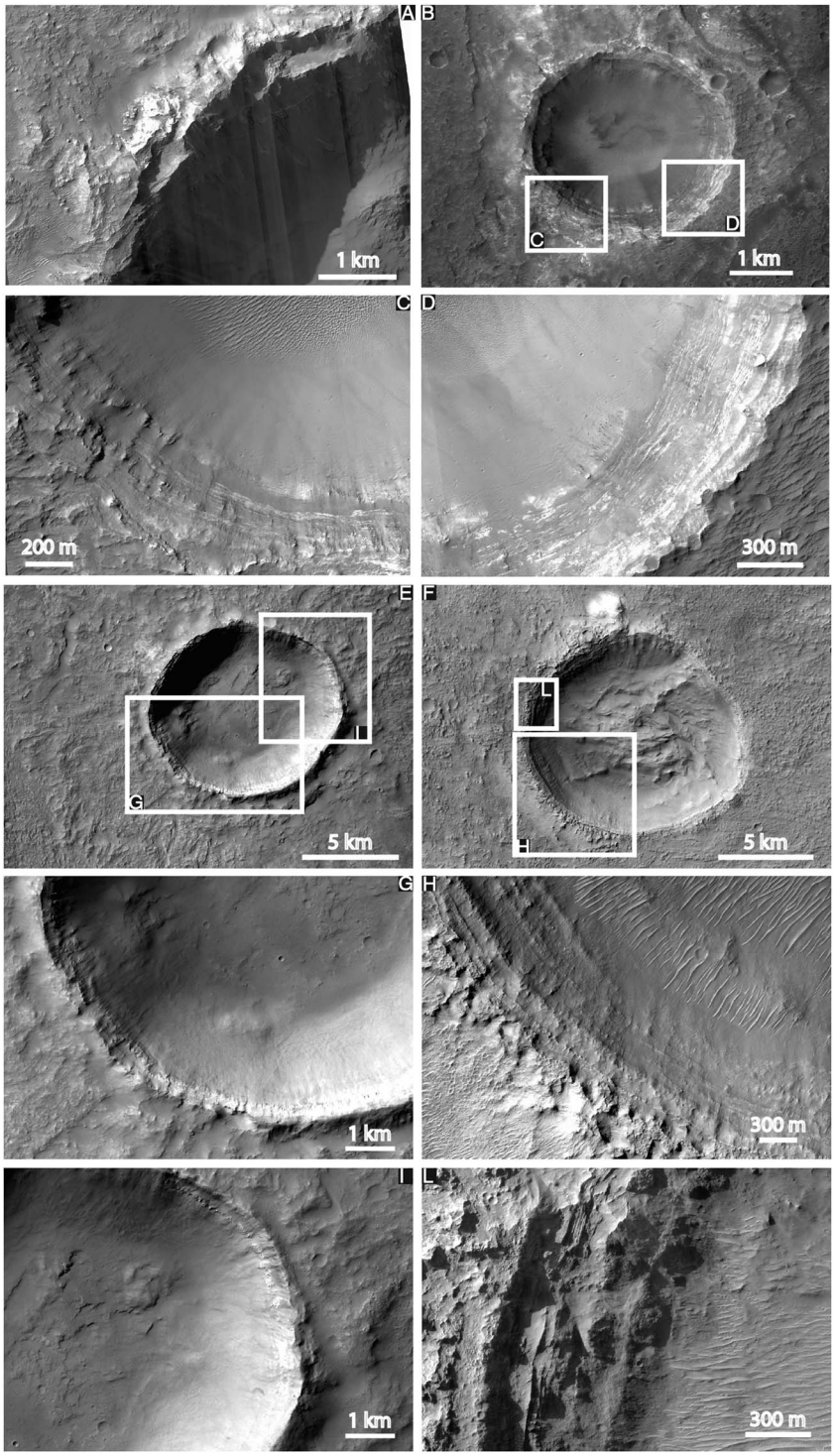

Figure 6. (a) Close-up of the light-toned layered crater rim shown in Figure 6c; image is from HiRISE frame ESP_036632_1550. (b) Crater excavated in light-toned layered rocks, which are interpreted as sedimentary in origin; image is from CTX frame F01_035999_1552. (c and d) Close-up of crater rims shown in Figure 6b, light-toned layered rocks are easily recognizable in these two figures; images are from HiRISE frame ESP_036421_1550. See text for explanation. (e and f) Impact craters in sedimentary rocks; images are from B17_016246_1593 and F02_036711_1575. See Figure 3b for context. (g) Close-up of southern part of crater rim in Figure 7a, the first few meters display the stratification of sedimentary rocks. (h) Well-stratified crater rim in sedimentary rocks, close-up of Figure 7b; image is from HiRISE ESP_036711_1575. (i) Close-up of northern part of crater rim in Figure 7a where light-toned layered rocks are visible. (l) Close-up of northern part of crater rim in Figure 7b, well-stratified sedimentary rocks are easily recognizable; image is from HiRISE ESP_036711_1575.

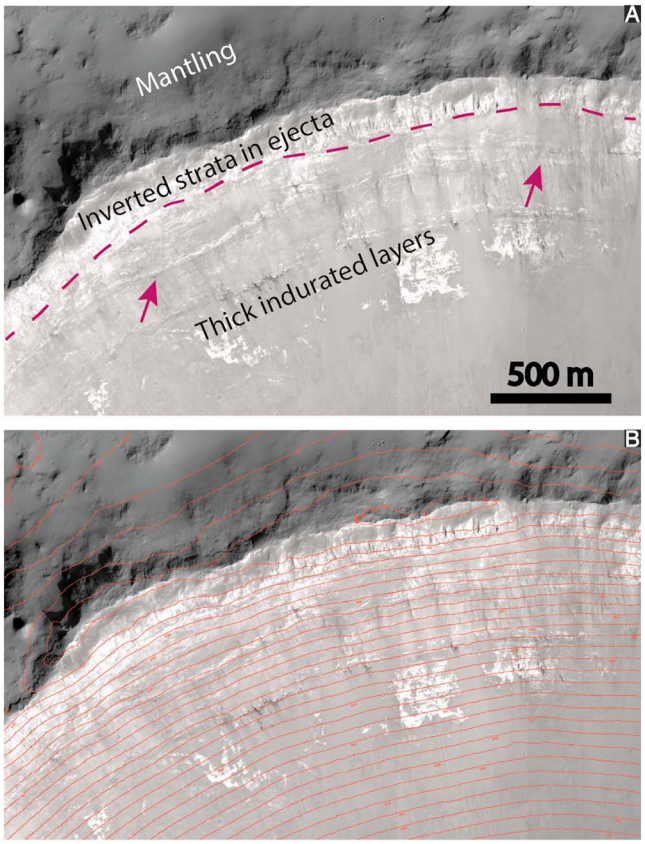

Figure 7. Well-stratified light-toned layered rocks interpreted as sedimentary in origin; HiRISE image ESP_027349_1555. Note that there are thick indurated layers and a concave-up layer set (arrows). (b) The same image on which HiRISE topographic contour lines with an interval of 25 m are superimposed. DEM is made from HiRISE stereo pairs ESP_027349_1555 and ESP_026861_1555, with a spatial resolution of 1 m pixel^{-1}. See Figure 3b for context.

material lithology, marked by an increase in protruding benches (e.g., fine-layered material without protruding (Figure 6) or layered material with outlined benches from which boulder rocks are falling (Figures 6g–6l)). The layer thickness is <10 m at the CTX scale, while layering at meter to submeter scale is visible at times with HiRISE (Figure 7). At the HiRISE scale, the layers generally display a relatively subplanar, subparallel, subhorizontal organization (Figure 7), but some concave-up layers are locally observed in association with local truncations (arrows in Figure 7), suggesting that deposit conditions changed locally.

Second, natural erosional windows are scattered in many places within intercrater plains, enabling the observation and identification of material lithology (Figures 3, 5d, 8, and 9). Despite their various shapes and dimensions (<100 s km^2), they display inner remnant buttes with flat summits (Figures 5d and 9a), suggesting that the inner structure of the material controls the erosion features. Note that few remnant buttes are circular, suggesting that material filled degraded craters were later eroded, forming inverted impact craters (south part, Figure 9a).

At the HiRISE scale, window material shows grooves, flutes, and yardangs, typical of eolian erosion in relatively weakly indurated fine-grained material (Figures 5d and 8). The window scarps or slopes generally display stacks of subparallel, subhorizontal, light-toned planar layers, which can be observed over several hundred meters in length (arrows in Figure 8b). For example, a dark layer that is sandwiched between light-toned layers can be followed both in the window escarpment and inside the inner crater rim (right side of Figure 8b).

Locally, cross bedding can be identified (Figure 9b) although most light-toned layers are parallel, subhorizontal, and do not display such facies. This suggests a change in lithology, favoring clastic deposits ranging from sand to pebble. In the upper part of the section (Figure 9b), decameter-large concave-up lenses are observed, in which curvilinear layers are arranged in a similar way to clastic sandy to pebble trough cross-bedding cut orthogonally to the flow path in aqueous terrestrial channels. There are many filled channels (outlined by arrows in Figure 9b) at the same elevation, suggesting that clastic sediments settled into ravine flows like in sandy braided-meander channels. These filled channels are themselves truncated by later deposits (white points in Figure 9b), as frequently observed in terrestrial channel sedimentary sequences. This sequence is repeated upward several times, suggesting a sedimentary context with aggrading channels and adjacent wetlands, possibly caused by a rising local base level.

In a few locations, light-toned layered material is also characterized by fractures and cracks. Local polygonal light-toned ridges separated by topographic depressions filled by dark sediment display a honeycomb pattern (Figure 8c). Honeycomb patterns can be due to weathering at the centimeter to meter scale, especially in the presence of water as observed with sandstones on Earth. Here the scale is both larger, with 10 m scale

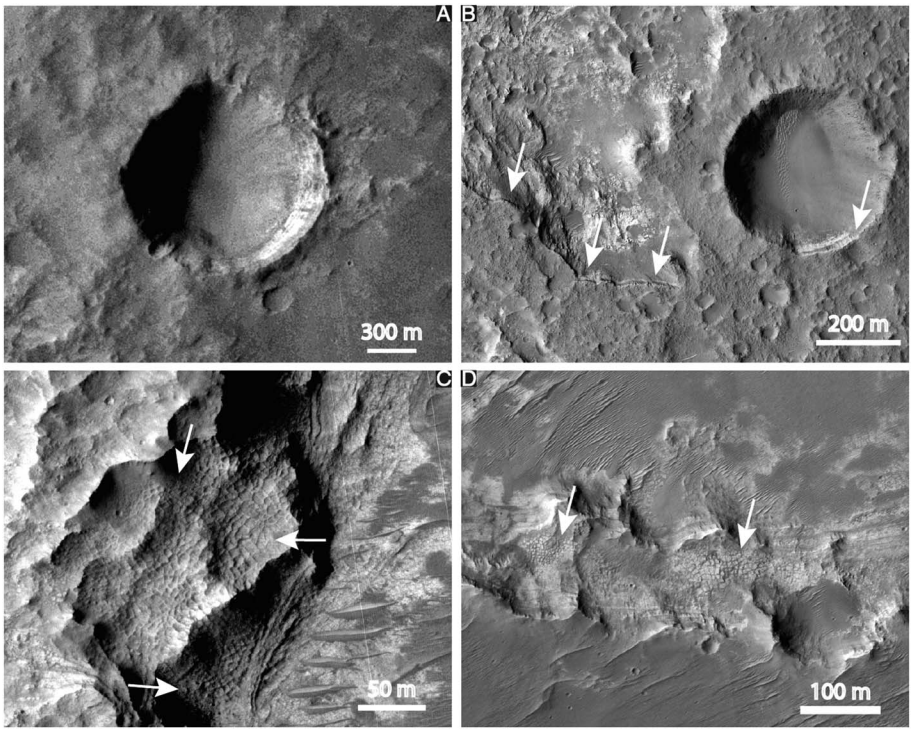

Figure 8. (a) Crater excavated in light-toned layered rocks, which are interpreted as sedimentary in origin (Context Figure 6c); image is from CTX D05_029116_1551. (b) Light-toned layered rocks, which are interpreted as sedimentary in origin, are observed in both the crater rim (Figures 8a and 8c) and erosional window (Figures 8b and 8d); image from HiRISE ESP_029116_1550. The dark layer on the crater rim, between the light-toned layers, can be followed on the escarpment on the left outside the crater (indicated by white arrows). (c) Light-toned ridges separated by topographic depressions filled by a darker material, which display a honeycomb pattern: boxwork structures (indicated by white arrows); image is from HiRISE ESP_029116_1550. (d) Weathering polygonal cracks (indicated by white arrows) in sedimentary rocks; image is from HiRISE ESP_029116_1550.

cells, and straighter. Although slightly different from those observed by *Siebach and Grotzinger* [2014], the resistant fracture networks in light-toned layered rocks could be consistent with boxwork structures, i.e., structures formed by mineralization in fractures that protrude after erosion. Nevertheless, variable grain sizes and composition can create similar patterns but only the grain size/composition follows a preexisting pattern genetically linked to diagenesis and then related to fluid circulation. Such a pattern is unlikely to result from the deposition of grains only.

In addition, crack systems with well-organized rectangles five- to six-sided polygons are visible locally (Figure 8d). These cracks are not resolved in the vertical resolution of HiRISE DEMs, so they are interpreted to be relatively shallow (<1 m). They are observed in each erosional window in the study area and are typical of the weathering of a weak (or hydrated) material, which we interpret as being distinct from lava flows that weather into more massive boulders [*Hon et al*., 1994; *El-Maarry et al*., 2014].

From all these geometric and geological characteristics, the fine-layered material is interpreted as sedimentary deposits (partially clastic) that were transformed into sedimentary rocks by diagenesis. The sedimentary rock extends down to 475 m in thickness in the deepest erosional windows and craters (Figure 7 and Table 1). This thickness is probably a minimum because no rough, massive substratum is observed at the bottom of erosional windows or craters. The minimum volume of layered deposits is estimated at ~125,000 km^3, considering the area covered by this sedimentary rock in intercrater plains.

4.2.2. Sedimentary Crater Floors

Ancient, highly degraded impact craters (>20 km in diameter of which only the rims remain) within the study area are commonly filled by light-toned layered deposits with the same characteristics as those observed in the erosional windows of the intercrater plains (Figure 10). These light-toned rocks are interpreted as being similar to those observed in the intercrater plains, suggesting a genetic connection between both types of

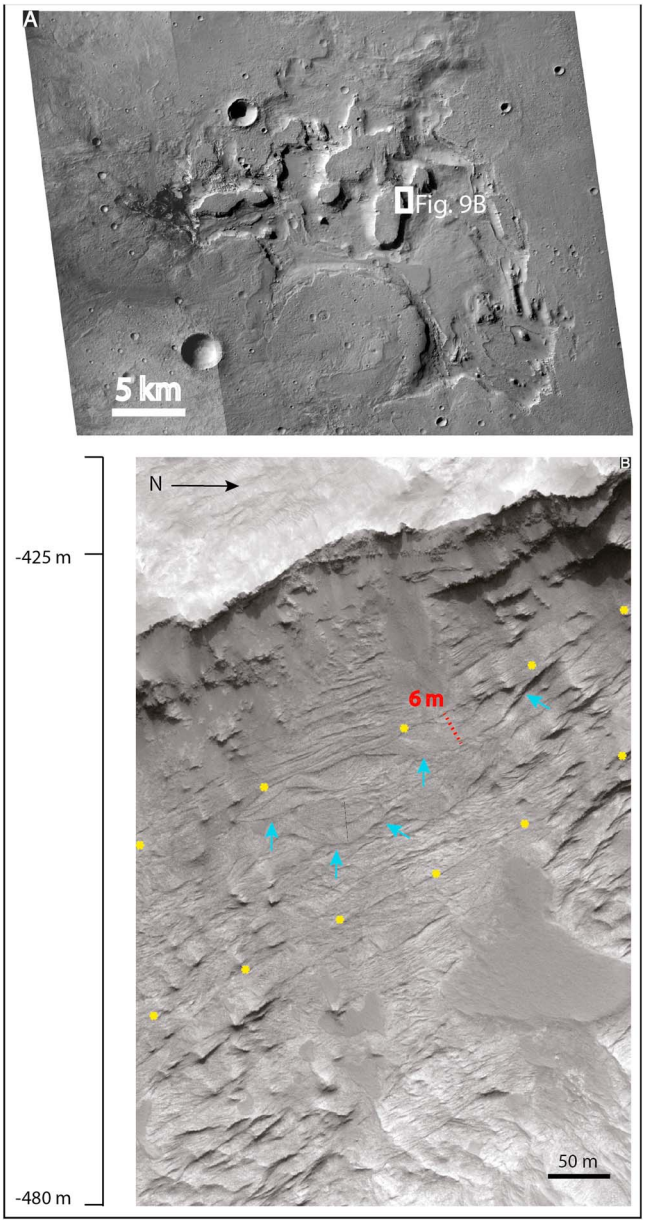

Figure 9. (a) Erosional window carved in sedimentary rocks; image is from CTX G21_026281_1539. See Figure 3b for context. (b) Cross-bedding stratifications in sedimentary rocks (sand-like grain size). White points display an extensive erosional surface underlain by truncated "lenses" outlined by light blue arrows. Possible buried channels. Image frame is from HiRISE PSP_003799_1540 with a resolution of 1 m pixel^{-1}. See text for explanation.

rock. In many places, a continuity of sedimentary rocks into intercrater plains is observed in large degraded impact craters with a sedimentary draping of the impact rim (e.g., the crater west of Niesten (Figure 3b) or other smaller degraded impact craters (Figures 8c and 10)). For the latter, it can be seen (along the bedding plane) that the layers dip toward the southeast with a slope of 3°, toward the crater, from the HiRISE DEM topographic contour lines of Figure 10. In the 3-D view of Figure 11, the inclined strata dipping toward the center of the crater can easily be recognized. Other smooth plains lacking erosional windows are thought to be sedimentary because their similar surface morphology, albedo, and stratigraphy are similar to those of the smooth plains interpreted as sedimentary. This is the case for several high-standing plateaus, but limitations in observations (no erosional windows, for example) are cause for caution regarding their interpretation. The topographic distribution of the sedimentary unit is very homogeneous, restricted to elevations between +500 m and −2000 m.

4.2.3. Minor Sedimentary Units

The relatively flat area, located on the outer Hellas rim, from the Schaeberle crater to the north of the Harris crater, standing between 0 and 1.5 km of elevation, is mapped as an undistinguished plain (dark green) (Figures 3a and 3b). It is a sedimentary unit because it is located at the southern boundary of highly cratered highlands incised by numerous branched valley networks that could have transported sedimentary material. However, this unit lacks exposures of bedrock (no windows and no fresh craters), so we are unable to provide more evidence for its sedimentary origin.

The unit of debris apron colluviums (green and orange striped unit, Figure 3a) corresponds to another minor sedimentary unit, located on relatively gentle hillslopes including ancient crustal buttes (brown unit). At the HRSC and CTX scales (Figure 4d), this unit is locally carved by shallow channels (<20 m deep), suggesting incision in a friable mantling (Figure 4a). This sedimentary unit is clearly younger as it lies inconsistently on various units and is probably unrelated to the larger sedimentary plains.

4.3. Volcanic Units

Several plains are mapped as volcanic plains (hatched purple units in Figure 3a). They stand at the same elevation as sedimentary ones and do not display erosional windows.

Table 1. Measurements of the Minimum Thickness of Sedimentary Rocks Using the Crater Shoulders as Natural Geological Cross Sections[a]

Location	Width (km)	Length, E-W (km)	Diameter (km)	Minimum Thickness of Sedimentary Rocks (m)
Crater Figure 6a	-	-	10.8	350
Crater Figure 6b	-	-	3.4	60
Crater Figure 6e	-	-	10.5	300
Crater Figure 6f	-	-	12	260
Crater Figure 7a	-	-	7.7	475
Crater Figure 8a	-	-	1.23	40
Crater Figure 8b	-	-	0	20
Erosional window Figure 9 (cross-bedding outcrop)	0.5	22	-	70
Erosional window Figures 10 and 11 (ghost crater infilling)	0.6	23	5	230
Erosional window Figures 17 and 19	0.4	65	-	350
-	-	-	-	
-	-	-	-	Average minimum
-	-	-	-	thickness: 210m
			-	
			-	

[a]Measurements of sedimentary strata thickness on the fresh crater (type III) in Figure 7a and in the erosional window in Figures 10 and 11 were made using HiRISE DEMs (with bundle adjustment), while CTX DEMs were used for other crater measurements. The value of minimum thickness of sedimentary rocks for the craters (type II) in Figures 6a and 6b is probably underestimated due to erosion of the upper part of the crater.

In visible images, these resistant terrains show no light-toned layered rocks but rather dark-toned, rough surfaces (Figure 12e). Specific landforms, distinct from those in the smooth sedimentary plains, are also observed. Two parallel ramparts indicate a several meters wide fissure in a topographic depression (Figure 12 a), which we interpret as a volcanic vent. Locally, there are also lobate shapes, interpreted as lava flow fronts, and ridges, interpreted as part of the lava flows (Figures 12b and 12c). Distinctive lava flow textures and the different degrees of surface degradation suggest that individual flows originate from separate eruptive events.

In nighttime THEMIS images, these volcanic terrains display a relatively high brightness temperature (Figure 12 f), suggesting a relatively strong rock cohesion or induration. The contact between lava flows and light-toned layered rocks (sedimentary intercrater plain unit) is well expressed in several areas where the rough, dark-toned material embays previous deposits (Figure 12d) but appears less obvious when the transition is obscured by mantling. Individually, these volcanic plains cover small areas (less than tens of square kilometers), with no lateral continuity and a total volcanic surface area of 34,000,000 km^2, i.e., 7.5 times smaller than that covered by sedimentary rocks. Local frontal lobes enable an estimation of the minimum thickness of lava flows to be ~20 m.

Volcanic flows are mapped in dashed purple (Figure 3) and cover a much smaller area (about 10 times less) than the sedimentary rocks. Their mapping only partly fits that of the smooth plains previously interpreted as volcanic from earlier maps [*Tanaka*, 1986; *Leonard and Tanaka*, 2001; *Tanaka et al*., 2014].

4.4. Craters and Crater Ejecta

Craters and their related ejecta are mapped in different colors according to their apparent degradation stage, being easier to identify than intercrater plains. The ancient crater rims, consisting of strongly degraded craters with superimposed fluvial landforms and devoid of an ejecta blanket, or with only poorly preserved ejecta (type I in the classification of *Mangold et al*. [2012]), are mapped in dark brown color. These craters are commonly filled by younger material (and mapped as light-toned sedimentary units in Figure 3).

Fresher craters classified as types II and III by *Mangold et al*. [2012] are mapped in different shades of yellow. Type II craters and their associated ejecta, which correspond to partly degraded craters with localized inner fluvial landforms, are mapped in dark yellow, while type III craters and their ejecta, which are fresh and lack any fluvial erosion, are mapped in lighter yellow. Type III craters are the best preserved with a continuous ejecta blanket and well-preserved rims.

5. Mineralogical Observations

The mineralogy of the geological units provided here aims to give a representative mineralogy of the key areas identified (sedimentary vs volcanic units) and not an exhaustive list of detections, which will be

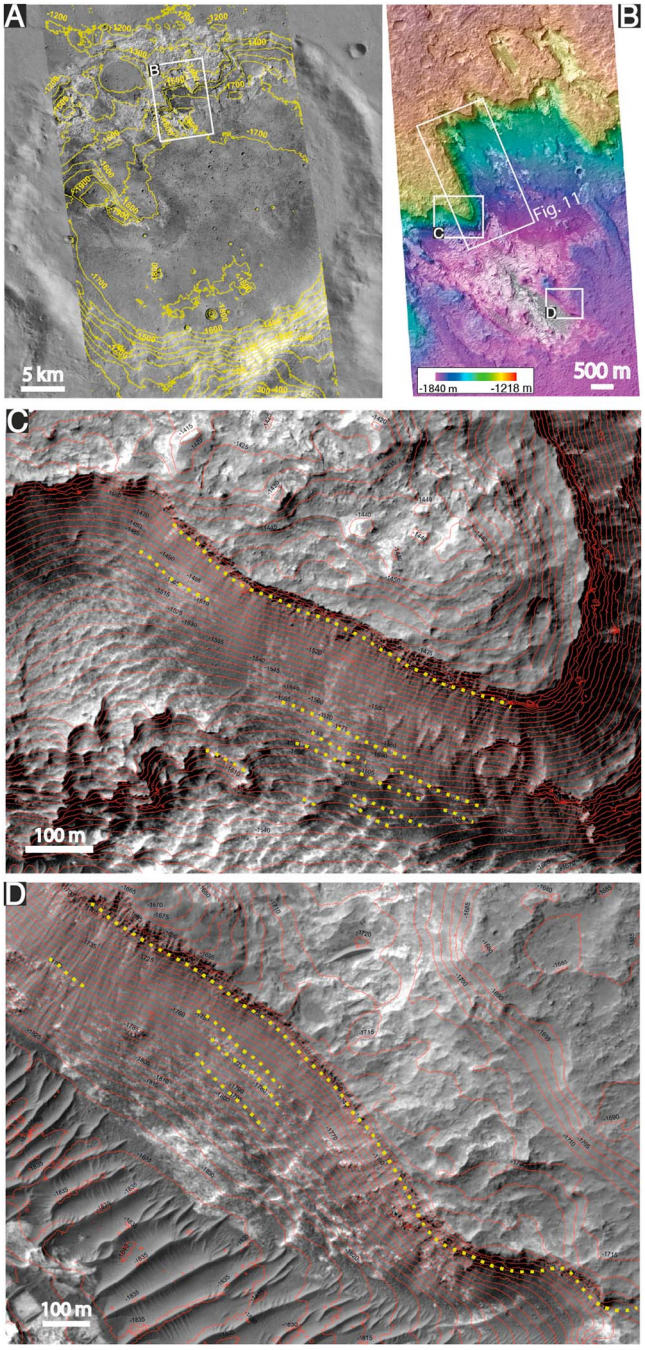

Figure 10. Layered light-toned crater-filling material. (a) CTX contour lines from images D16_033520_1530 and D16_033454_1530 around resolution 6 m pixel^{-1}. (b) HiRISE DEM with bundle adjustment (HiRISE stereo pairs ESP_033454_1545 and ESP_033520_1545) with a resolution of 1 m pixel^{-1}. (c and d) Close-ups of HiRISE image, centered on erosional windows in filled degraded impact crater, on which topographic contour lines are superimposed. Scarps show layered rocks, outlined by dashed yellow lines, with low dips differing from the horizontal. These dips may be the result of sediment deposition on gentle slopes within this ancient crater.

provided in a companion paper in preparation. The mineralogy was investigated using high-resolution "targeted" observations from the CRISM imaging spectrometer. These provide limited coverage of each unit (<1%) at high spatial (<40 m/pix) and spectral (<7 nm) sampling. To account for this poor coverage, a sample of several tens of targets was acquired and analyzed over each unit to provide reliable trends. All the available targeted observations within the region of interest were analyzed, and representative spectral signatures and mineral maps are shown in Figure 13. The calibrated surface radiance is converted into reflectance and then normalized to highlight the weak aqueous mineral signatures when present, as described in *Carter et al.* [2013b]. A number of spectral indexes are used in combination to search for different types of aqueous minerals based on their diagnostic absorption features in the near-infrared (1.2–2.6 μm). These indexes provide a qualitative assessment of the presence or absence of specific minerals and are based on simple spectral band math, which measures the depth of an absorption band or shoulder (when one sided). They are used in combination to increase their specificity for given minerals that have known correlations of absorption features, while efficiently rejecting false positives due to observational biases or noise.

Contiguous pixels with positive index values above an empirically adjusted threshold are considered detections. This overall threshold is determined by incrementally increasing the minimum tolerated absorption band depth for each spectral index until the corresponding index map does not exhibit false positives upon inspection of the spectra. These pixels are then median averaged, from which a high signal-to-noise spectrum is extracted. They are then compared visually to laboratory spectra of known terrestrial analogs.

As elsewhere on Mars, the aqueous mineralogy is dominated by varieties of Fe/Mg phyllosilicates (Figure 13) as

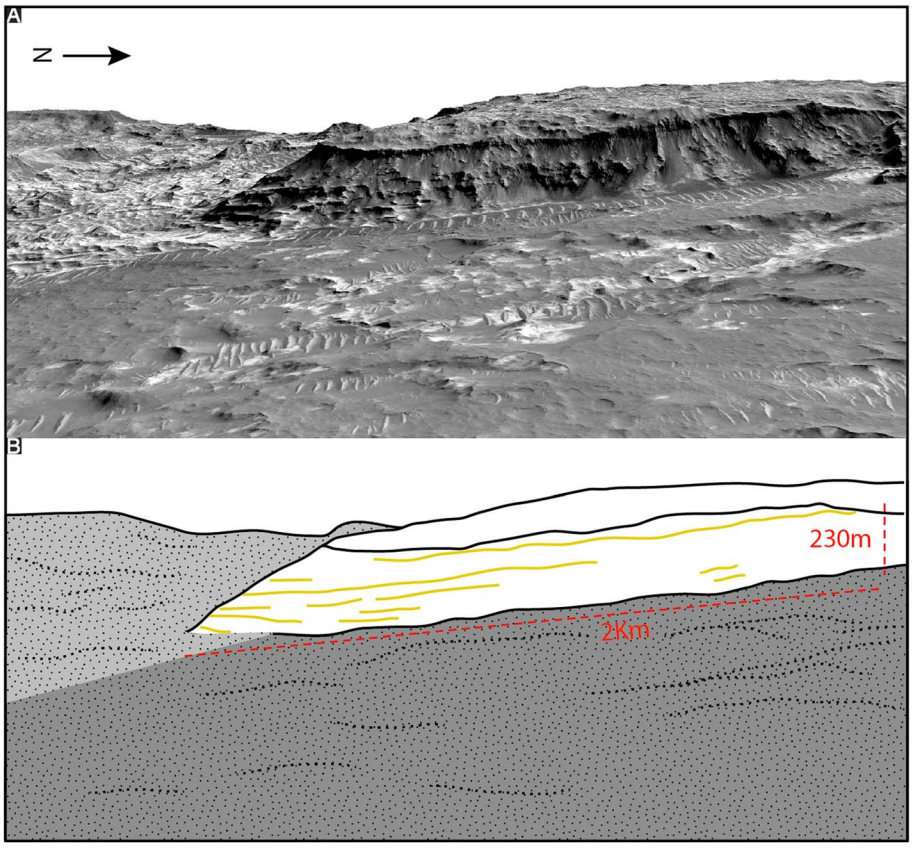

Figure 11. (a) Three-dimensional view of sedimentary deposits filling the crater in Figure 10 (HiRISE stereo pairs ESP_033454_1545 and ESP_033520_1545 and HiRISE DEM with a resolution of 1 m pixel^{-1}). The outcrop is 230 m thick and 2 km long. (b) White lines, sketch of sedimentary layers, the dip is toward S/SE, toward the crater center and the Hellas basin.

identified by their prominent mineral absorption(s) in the 2.25–2.4 μm range [*Bishop et al*., 2009]. As discussed below, subtle variations in the position, shape, and number of absorption features in this range provide additional insight into their mineral composition and structure.

Numerous clay mineral detections occur in the northern Hellas rim, and strong correlations are found between the phyllosilicate absorptions and the geological units as mapped in *Carter et al*. [2011]. In particular, phyllosilicates are detected in all the targeted planar light-toned layered rocks in erosional windows (e.g., Figure 13) and inside fresh crater rims. Exposed sediments from erosional windows systematically exhibit a similar set of spectral features illustrated in Figure 13. These are characterized by (i) an Fe/Mg-OH band at 2.30–2.305 μm, which is sharply asymmetrical (left-sided shoulder) and rounded; (ii) an H–O–H band at 1.90 μm comparable in depth to the Fe/Mg-OH band; and (iii) additional minor bands at 1.40 μm, 2.39 μm, and rarely at 2.25 μm. These correspond to the most common clay signatures on Mars and have been interpreted as either pure smectites or mixtures of smectites and micas. Based on the available library spectra, these are best matched by vermiculite mica and Mg- or Fe-rich saponite smectite (see laboratory spectra in Figure 13). If only a purely smectitic contribution is considered, then these clays fall within "Group 3" of the classification of *Michalski and Smith* [2015], corresponding to an Fe/Mg ratio of 5–10 and a dioctahedral or mixed layer ditrioctahedral structure. Some spectra exhibit a weak additional Al/Fe-OH band at 2.25 μm, indicative of tetrahedral Al^{3+}/Si^{4+} substitution or octahedral Al^{3+} in smectite or mica/vermiculite (e.g., second from top spectrum in Figure 13).

The few CRISM observations covering the volcanic unit (Figure 3) show no evidence of hydration signatures, consistent with the lower resolution OMEGA regional mapping.

Both CRISM and lower resolution, full coverage observations with OMEGA (Figure 14) [*Bibring et al*., 2004; *Ody et al*., 2012] show predominantly pyroxene signatures in the volcanic units identified from morphological

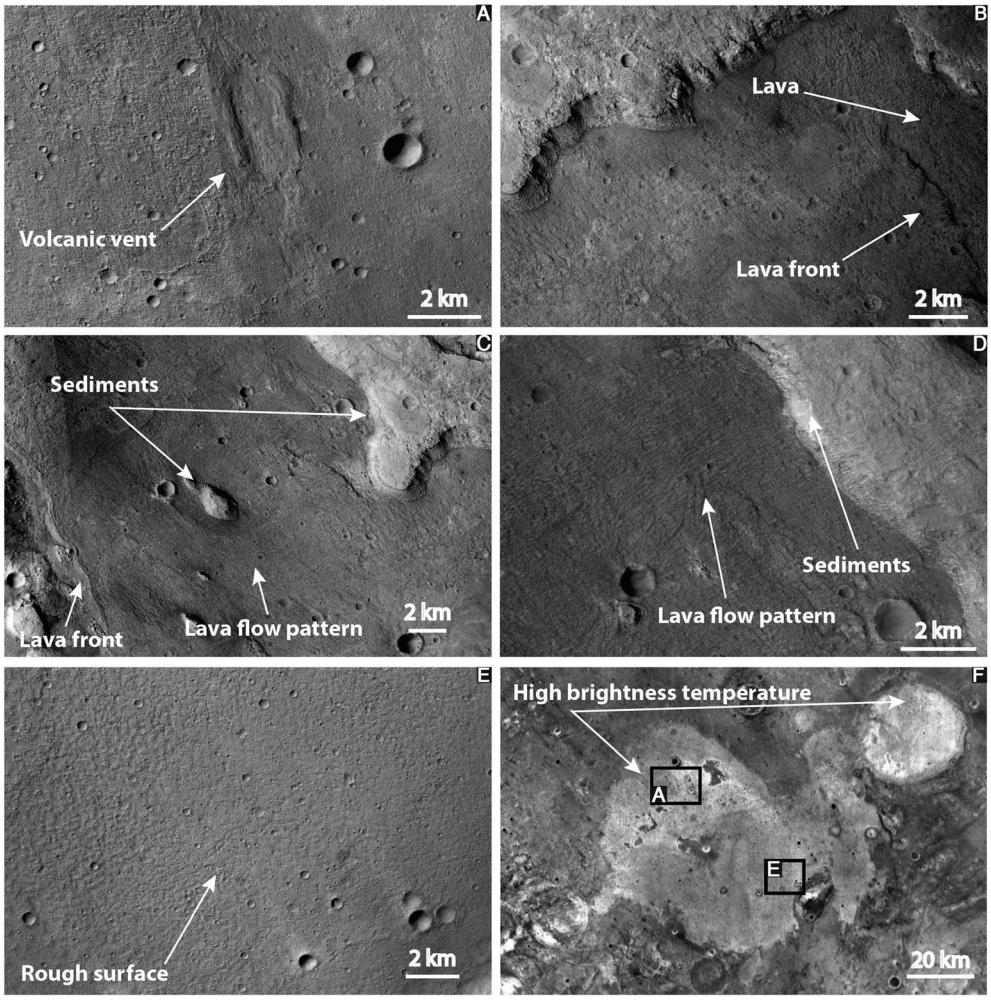

Figure 12. (a) Volcanic vent with low ramparts on both sides of the fissure; image is from CTX B03_010642_1561 and P22_009719_1561. Context Figure 12f. (b) Lava flows and related lava front (dark sediment) onlapping light-toned rocks (sedimentary in origin); image is from CTX F07_038650_1532. (c) Lava flows inside the erosional window onlapping sedimentary rocks. The remnant butte at the center of the image is light toned and bedded like the main sedimentary rocks; image is from CTX F07_038650_1532. (d) Well-preserved onlap contact between volcanic flows and sedimentary rocks. (e) Rough surface of volcanic flows; image is from CTX F07_038650_1532. Context Figure 12f. (f) THEMIS image showing high brightness temperature terrains that correspond to the volcanic flows (Context Figure 3b for Figures 12b–12d and 12f).

analyses. Figure 14 displays a good match between the pyroxene-rich region of the OMEGA map (in red in Figure 14d) and the volcanic units (purple color in Figure 14a). However, west of the volcanic unit, the modal abundance of pyroxene remains relatively high despite being at the location of sedimentary plains (green). In these locations, there is no outcropping material of layered rocks but a dark eolian blanket, which may correspond to volcanic material blown by wind over these plains. No strong signature of olivine is identified within these units. The strong pyroxene signatures within the volcanic unit may mask minor contributions from olivine, and/or the basalt itself may have been depleted in olivine. Olivine is found in the greater northern Hellas region but is mostly restricted to ancient buttes where it is interpreted as material excavated from the upper mantle/lower crust during the basin-forming event [*Ody et al.*, 2013]. Fe-rich plagioclase, the only variety directly detectable within this spectral range, is not found associated with any of the units described here.

Overall, the mineralogy data presented are consistent with the distinct nature of the two types of smooth plain: pyroxene-bearing lava flows and phyllosilicate-rich light-toned rocks.

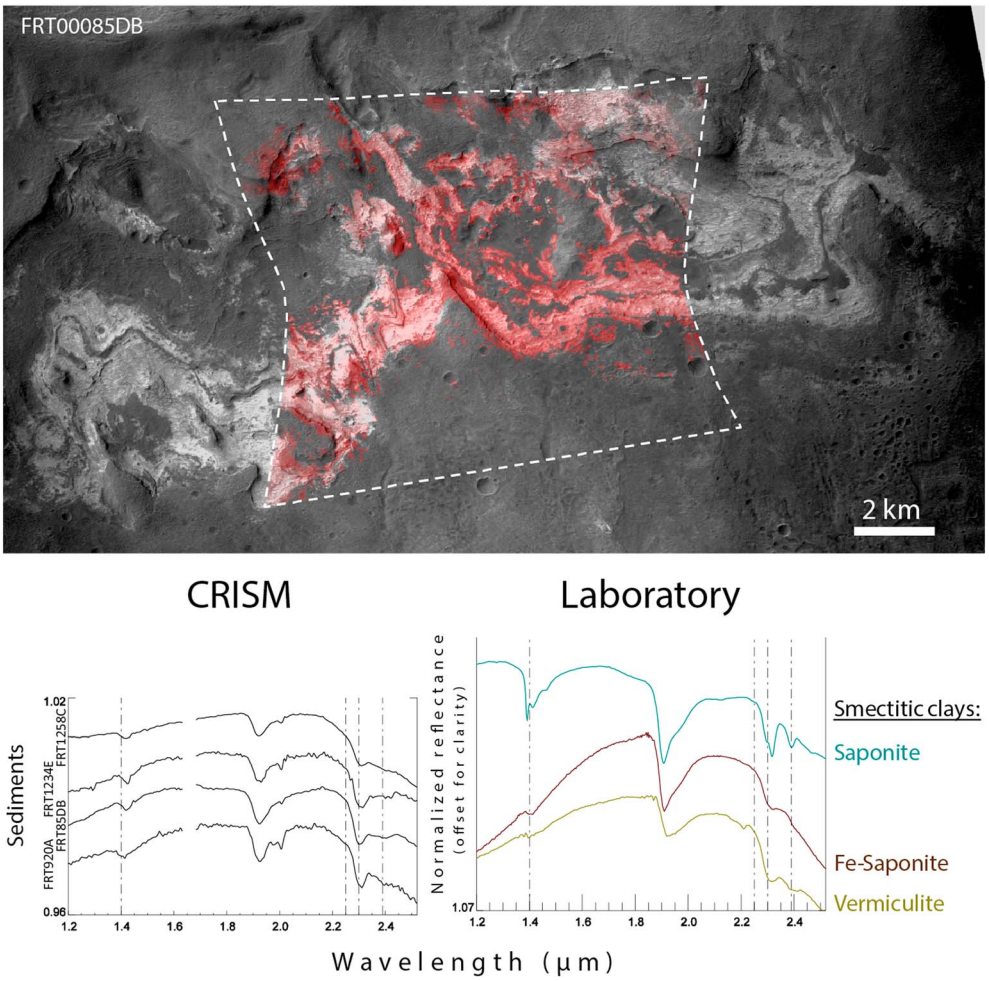

Figure 13. Example context for CRISM detections of Fe/Mg phyllosilicates (mapped in red over CTX). (top) Example mineral map of the smectitic clay signatures in sediments exposed within an erosional window. Observation FRT000085DB was used. (bottom left) Four representative normalized Fe/Mg phyllosilicate normalized reflectance spectra based on CRISM observations within the sediments (see vertical axis for the corresponding observation numbers). (bottom right) Candidate laboratory spectra of different mineral families providing best matches to each spectral type. Context Figure 3b.

6. Stratigraphy

6.1. Relative Stratigraphy

In order to understand better the geological timing and depositional mechanisms of the sedimentary and volcanic plain units, their relative stratigraphy was investigated throughout the region (Figures 3 and 15). CTX visible images were used to understand the stratigraphic relationships at the regional scale, and HiRISE DEM and visible images were used to investigate more thoroughly the stratigraphy and stratigraphic relationships of volcanic and sedimentary rocks. Both types of plain are younger than the remnant buttes, mapped in brown color and interpreted as ancient crustal bedrock, because plain materials onlap the toe of buttes and never drape them (Figures 3 and 14–16). In a few places, volcanic plains (Figure 3) embay the toes of remnant buttes, surrounding their lower sides (Figure 14a). Sedimentary plains, characterized by fine-layered material in the erosional window scarp (Figure 16), show an onlap contact at the toe of remnant buttes (white arrows in Figure 16), as observed in a well-preserved area to investigate stratigraphic relationships (Figure 15). All these observations show that remnant buttes not only predate volcanic and sedimentary plains but also never covered by their respective material (Figure 15).

Understanding the stratigraphic relationships between sedimentary and volcanic units requires more detailed observations of their contacts. Figure 15 shows a well-preserved area to investigate them. In daytime

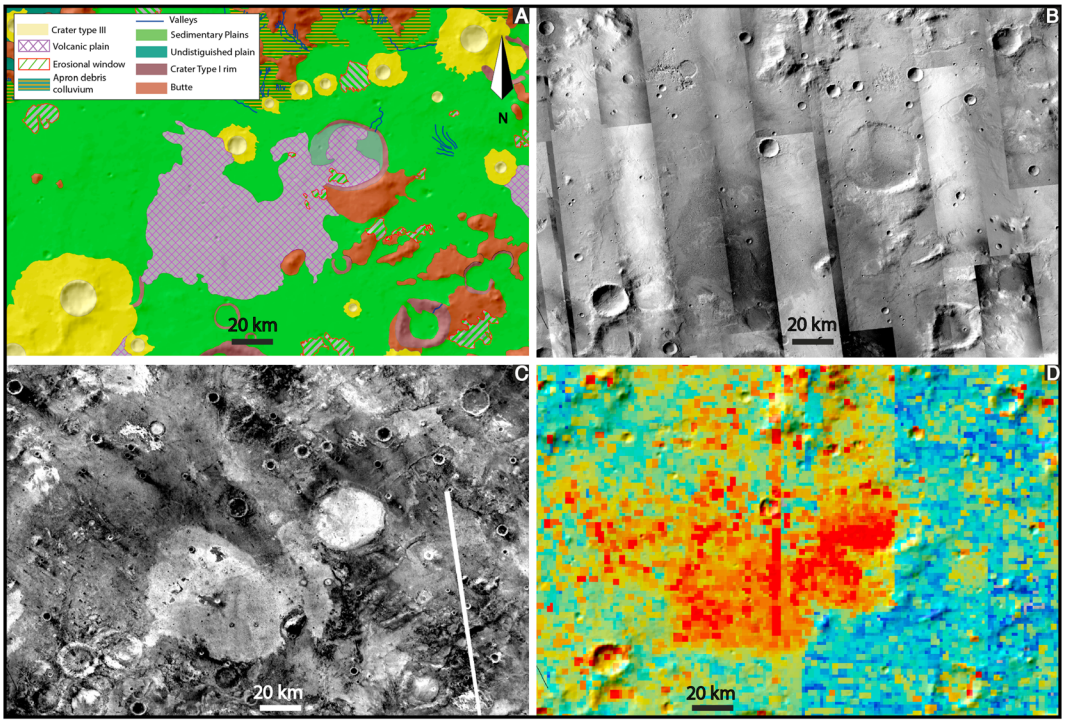

Figure 14. (a) Geological map showing smooth plains (light green) and volcanic flows (purple). (b) CTX images showing dark deposits in the middle corresponding to the purple unit on the geological map and light deposits that are mapped as sedimentary rocks on the geological map. (c) THEMIS image showing high nighttime brightness temperature terrains that correspond to the volcanic units. Sedimentary rocks are characterized by a medium to low nighttime brightness temperature. (d) OMEGA images showing a high concentration of pyroxenes matching volcanic flows (red pixel). OMEGA data also show pyroxene over sedimentary rocks, which could be due to sediment eroded and transported there by the wind. See Figure 3b for context.

THEMIS images (Figure 15a), volcanic plains appear relatively dark and cover the central part of the figure, whereas sedimentary plains seem relatively brighter. The panoramic view of this area (Figure 15b), made by a CTX mosaic superimposed on MOLA topography, shows an oval topographic depression from which small tabular hills rise. At the northeast part of this depression, one 18 km diameter degraded impact crater shows an undulating scarp.

Figure 17 displays a close-up of the topographic depression identified previously (Figure 15b). It is embayed by lava flows, marked by features of flows and lava fronts (Figures 17a and 17c), suggesting that the volcanic flow came from the western side of the depression. The volcanic filling inside the depression is characterized by (at least) two volcanic events: lava flow 1 and lava flow 2 (Figure 17c), which display two corresponding lava fronts. Locally, lava flows surround the toe of small, tabular, light-toned hills (Figure 17c) and are stopped by onlap contact on the toe of the depression scarp (Figures 17a, 17b, and 17d), implying that they postdated the depression formation.

The inner tabular hills and depression scarp are composed of relatively continuous, light-toned layered material (Figures 17b–17d and 17f), interpreted as sedimentary rocks (Figure 15c). The thickness of these rocks ranges from 100 m in western side of the depression to 350 m near the degraded impact crater (Figure 17).

In addition, thin volcanic lava flows, < 20 m thick (Figure 17d), overlap the outer sides of the depression, above its sedimentary scarp. Locally, thin volcanic flows are degraded and eroded (Figures 17d and 17e), showing outcrops of sedimentary rocks outside the depression (e.g., surroundings of the impact crater (Figures 17a and 17b)). Thin lava flows at the summit of the sedimentary scarp belong to the same volcanic events as observed inside the depression, as shown on the geological map (west side of box #4, Figure 15c). Once again, lava flows postdated sedimentary rocks.

From these observations, we conclude that (i) sedimentary rocks formed before volcanic rocks and (ii) sedimentary rocks were eroded, yielding an oval depression containing remnant tabular hills.

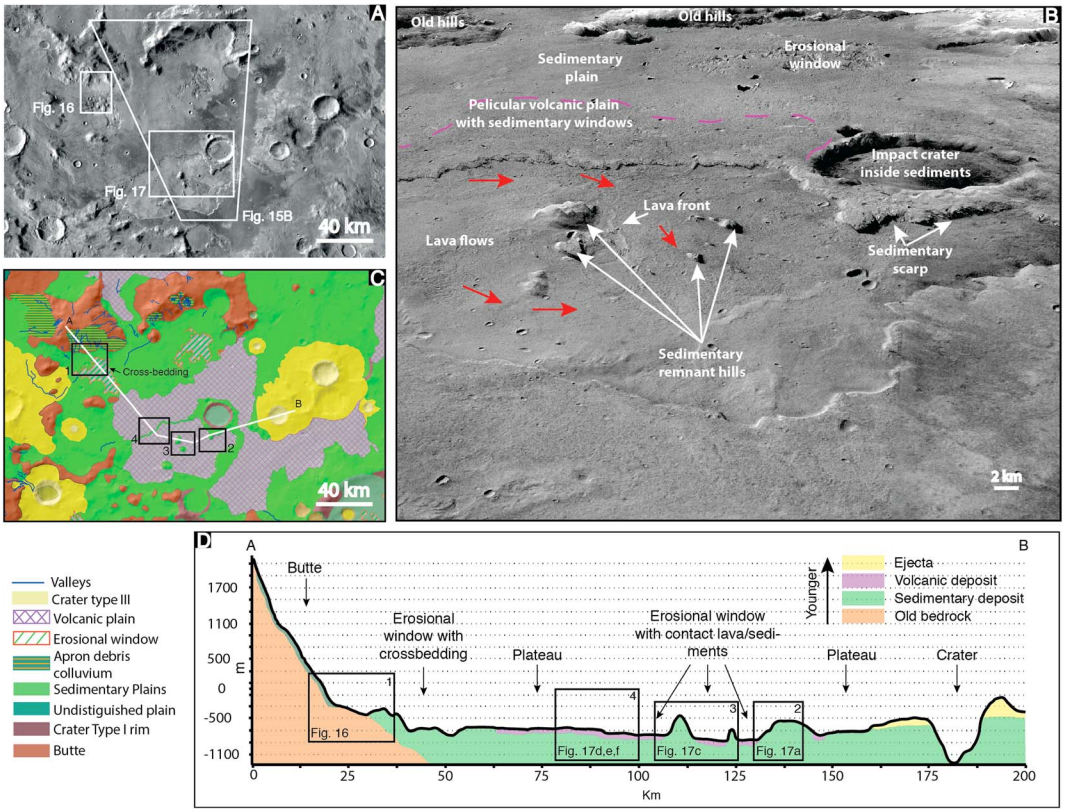

Figure 15. Relative stratigraphy between the different units. See Figure 3b for context. (a) Daytime THEMIS image showing morphology of different geological units mapped in Figure 15c (hills, sedimentary and volcanic plains, impact craters, and their ejecta). (b) Three-dimensional view of the area, including hills, plains, erosional windows, and impact craters with their interpreted lithology. Mosaic of CTX images draped on MOLA topography. (c) Geological map. (d) Geological cross section showing the relative stratigraphy of the geological units. Black boxes show the location of figures arguing for chronological relationships and their number corresponds to their location on the geological map viewed in Figure 15c.

Based on the geological map (Figure 15c) and MOLA topography, a geological cross section (Figure 15d) displays the chronological relationships between the major geological units.

Remnant buttes (brown unit), composed of old crustal bedrock, are surrounded by onlapped sedimentary plains (box 1). The latter is locally eroded, forming erosional windows and depressions, from which remnant hills rise (boxes 2 and 3). After this intense erosion stage, thin volcanic material overlapped sedimentary plains, forming volcanic plains.

This example illustrates a cyclical history beginning with the deposition of sediments, followed by a phase of erosion that created the erosional windows. Finally, volcanic flows draped the partially eroded sedimentary rocks. Erosion and deposition after the volcanic flow emplacement may have been limited in order to explain the preservation of these contacts inside the erosional windows.

6.2. Crater Retention Ages

Crater counts were carried out on sedimentary and volcanic units to estimate the relative time sequence of events and their individual absolute model ages of formation (Figure 18). The age of sedimentary rocks was calculated on five areas of the studied region as shown in Figure 18b. Figure 18a represents the average age of the sedimentary rocks from the sum of all these crater counts. In general, crater size-frequency distributions over the diameter range used are only marginally influenced by crater modification at a small size, as they correspond well to the isochrons of *Ivanov* [2001]. The youngest volcanic unit investigated has a crater retention age of $3.29+0.12/-0.21$ Ga (Late Hesperian). Given the representative number of craters >1 km, we interpret this crater retention age as being close to the model age. The sedimentary unit exhibits a model age of $3.70+0.03/-0.04$ Ga (Noachian). This marks the end of the depositional activity, as the earliest deposits that are now buried cannot be dated.

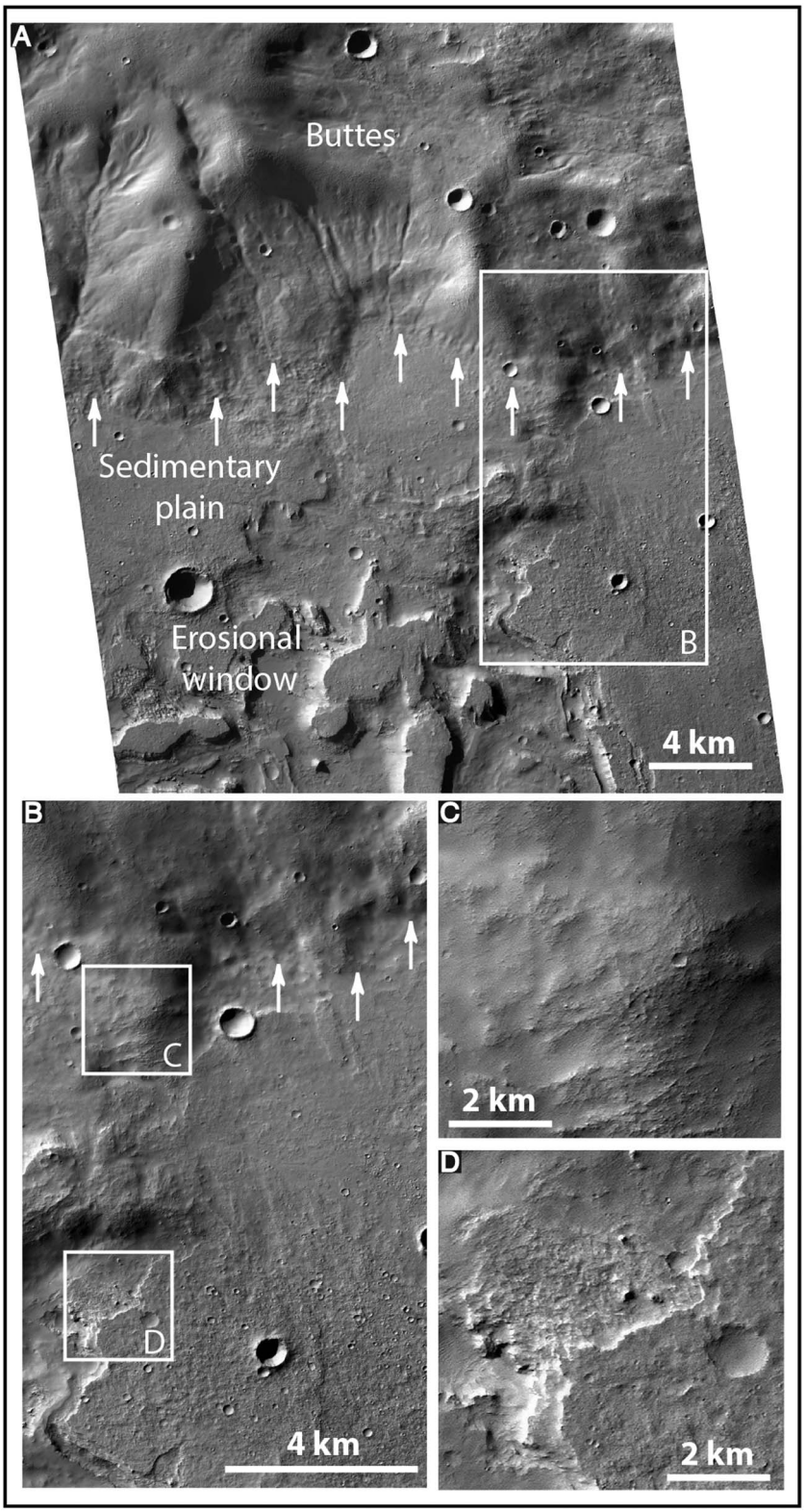

Figure 16. (a) Stratigraphic relationships between buttes and sedimentary plains. See Figure 3b for context. (a) CTX image showing the onlapping boundary of sedimentary plains on buttes (white arrows). (P22_009640_1543). (b) Close-up showing the deflation surface of layered sedimentary plains with (c and d) ventifacts and flutes shown in detail.

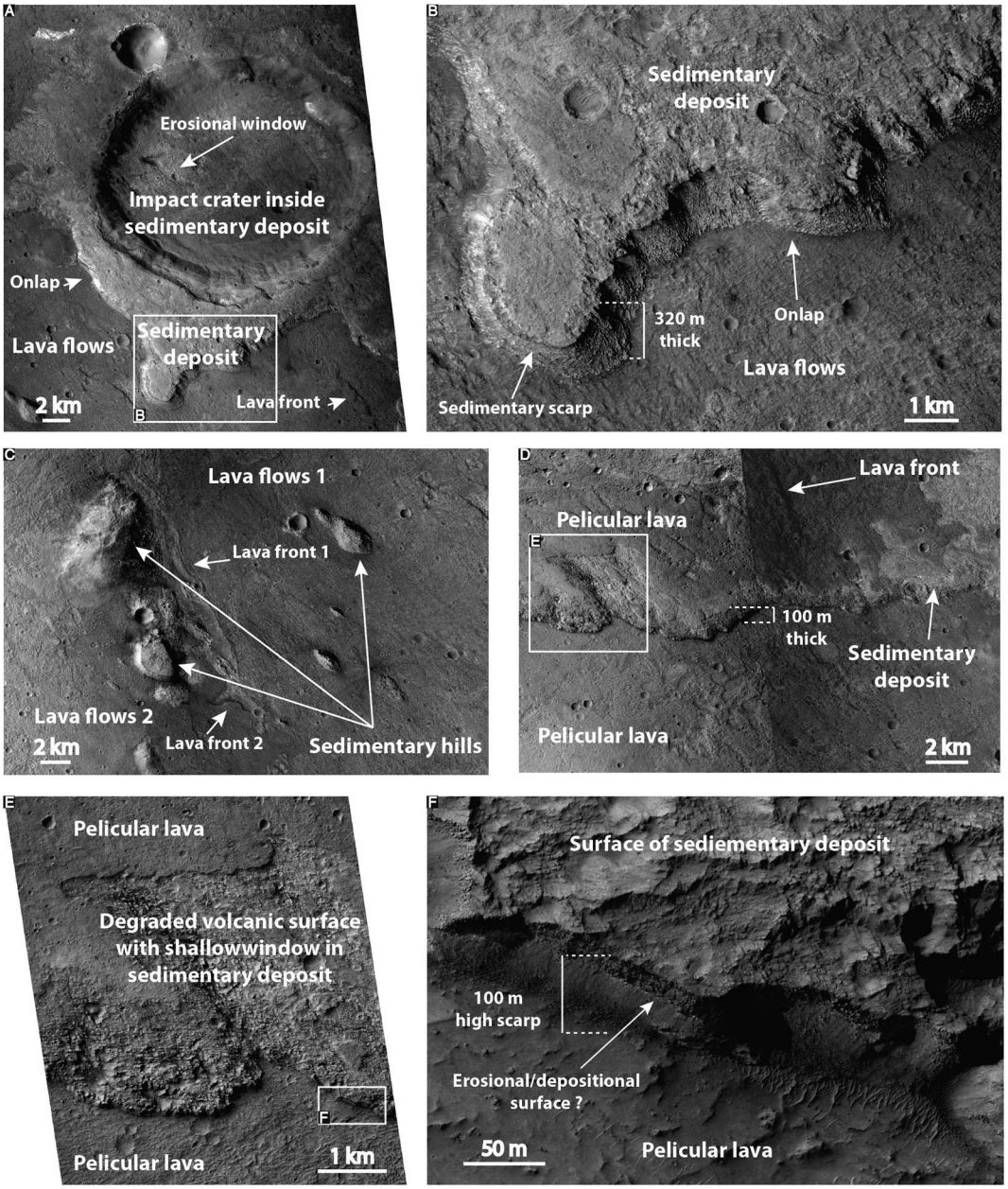

Figure 17. Stratigraphic relationships between volcanic and sedimentary plains in an erosional window. (a) Degraded, 20 km diameter impact crater inside layered sedimentary rocks shows a layered scarp at the southern outer edge. The scarp toe is overlapped by rough, low-albedo lava flows (CTX F07_038650_1532). (b) Close-up of the lava flow onlapping the toe of the 320 m high sedimentary scarp. (c) Close-up inside the erosional window displaying remnants of sedimentary hills and two different volcanic events with their related lava fronts. (d) Close-up showing stratigraphic relationships; volcanic lava flows (upper image side) that overlapped both the summit of a stack of 100 m thick sedimentary deposit, marked by a layered scarp and the floor of the erosional window (lower image side); image is from CTX G15_024224_1535 and B11_013965_1531. (e) Close-up showing erosion of lava flows at the top of the layered scarp; image is from HiRISE ESP_027758_1530. (f) Close-up of sedimentary deposit showing possible erosional/depositional surface inside the layered deposit.

Using the smaller crater population enables the actual surface age of the deposits, after their partial erosion, to be characterized. Resurfacing processes overprinted the entire studied area until $3.25 + 0.04/-0.06$ Ga. Interestingly, this age is of the same order as that of the volcanic flows, showing that the erosion that carved the erosional windows had mostly finished at the time of the volcanic episodes (Table 2), as suspected from stratigraphic observations.

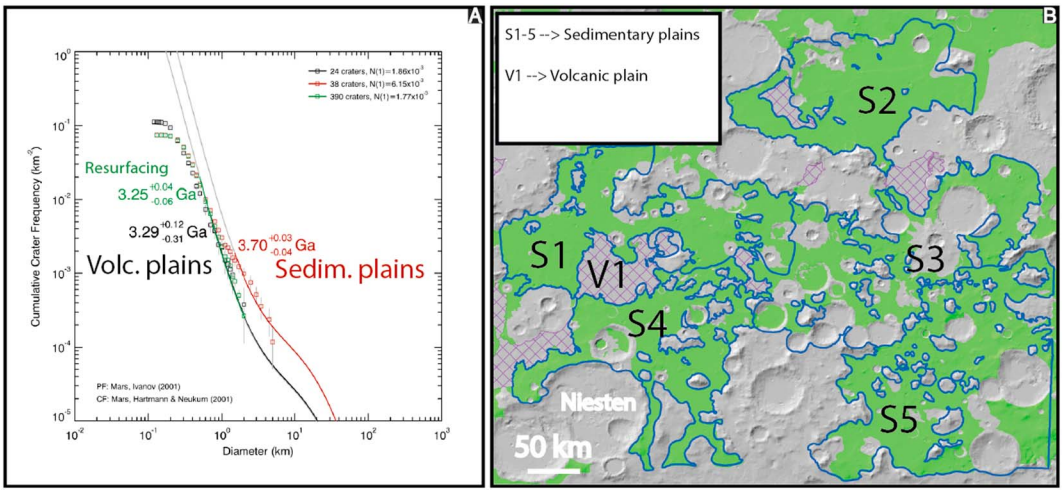

Figure 18. (a) Cumulative crater size-frequency distribution plots for all investigated key units. Solid red line: Isochron fitted to diameter bins interpreted as containing primarily craters, which have accumulated on the sedimentary surface. Solid black line: Isochron fitted to diameter bins interpreted as containing primarily craters, which have accumulated on the volcanic surface. Solid green line: Isochron fitted to diameter bins interpreted as containing primarily craters, which have accumulated after a certain resurfacing of the sedimentary unit. (b) Sedimentary (S#) and volcanic plains (V#) on which craters were counted. Age of sedimentary rocks is the average of the dating of the five smooth plains.

6.3. History of Deposition and Erosion Rates

The history of the northwestern rim of the Hellas basin can be summarized using the locations where volcanic and sedimentary plains are in contact (e.g., Figure 15). The regional geological cross section and stratigraphic column in Figure 19 provide a full summary of this history: (i) crustal rocks uplifted by the Hellas impact, (ii) Late Noachian sedimentary rocks covering the ancient crust of the northern Hellas rim with the exception of residual buttes and ancient crater rims, and (iii) Hesperian volcanic flows locally covering the sedimentary rocks. The erosional windows are due to the strong erosion of the sedimentary rocks, which occurred before their partial filling by lava flows. Inside the erosional windows, there are buttes that are remnants of the sedimentary unit. In the topographic profile (Figure 19c), it can be seen that the top of the residual buttes in the erosional window is at the same altitude as the sedimentary unit on the plateau, near the hills unit in the west and near the crater rim to the east. A green dotted line has been drawn to show the former location of the upper sedimentary surface at the end of the depositional period, ~3.7 Ga. Sediment thickness is estimated at a minimum of 350/400 m. Any deposition rate would be too speculative as the duration of the deposition period is unknown. Nevertheless, such a thickness may be consistent with the fluvial erosion that Mars experienced in the Late Noachian and remains consistent with locally thicker rocks observed regionally, i.e., 2 km thick rocks in the Terby crater [*Wilson et al.*, 2007; *Ansan et al.*, 2011].

The geological process that can be quantified is the erosion rate postdating the end of the sedimentary deposition. In this area, the volcanic unit sealed the erosional windows in sedimentary rocks at ~3.3 Ga. Knowing the initial thickness of the sedimentary rocks eroded, their age, and the upper sedimentary surface, we can estimate that the minimum erosional rate of ~400 m in 400 Ma is equivalent to ~1 m/Ma at the Noachian-Hesperian transition. This erosion rate is a minimum because most of the erosion could have occurred shortly after the deposition and not over the entire period of 400 Ma. Furthermore, the erosion rate calculated in the area in Figure 19 is not an average rate of denudation but a local rate. Given the poor erosion observed after the volcanic flows, this erosion rate seems to have dropped significantly in the Late Hesperian, <3.3 Gy.

Table 2. *Ivanov* [2001] Chronology Related in *Hartmann and Neukum* [2001] and Used in This Work

Epoch	Time, Ga (Hartmann)
Early Noachian	>3.85
Middle Noachian	3.85–3.75
Late Noachian	3.75–~3.55
Early Hesperian	~3.55–3.35
Late Hesperian	3.35–2.9
Early Amazonian	2.9 - 1.4
Middle Amazonian	1.4–0.3
Late Amazonian	0.3–0

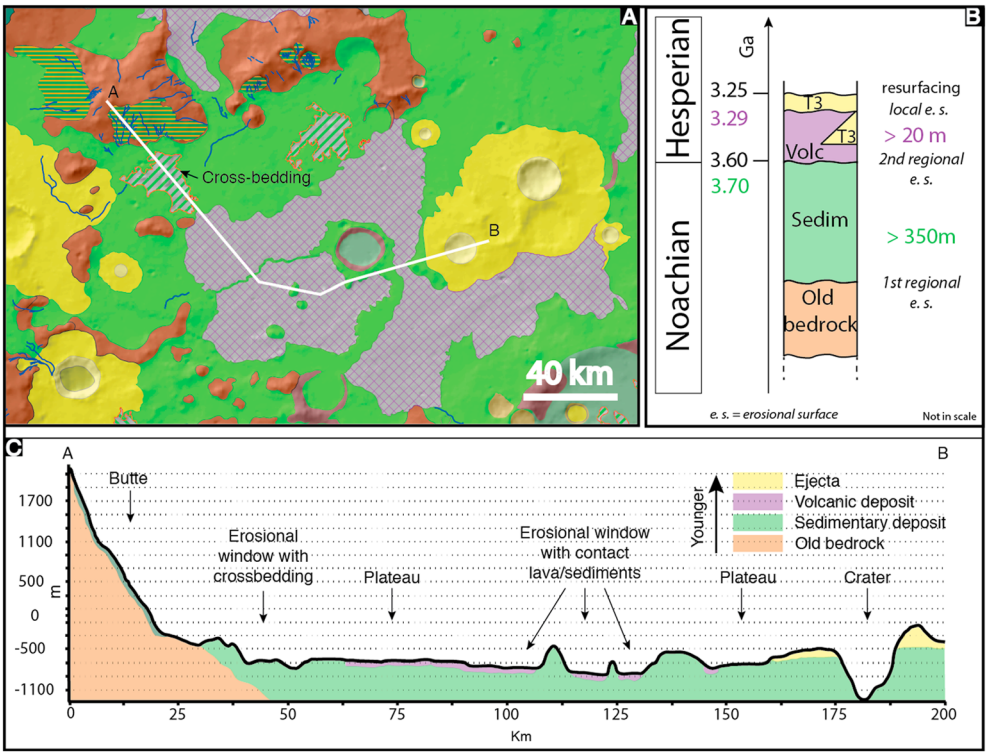

Figure 19. Synthetic geological history of the NW part of the Hellas basin from a particular erosional window north of the Neisten crater, see Figure 3b for context: (a) Geological map showing all the main units and cross-bedding outcrop inside the erosional window. (b) Stratigraphic column showing the main units of the studied area. In this region two main regional erosional surfaces are recognized, one between old hills and sedimentary rocks and another, more recent between sedimentary rock and volcanic flows. Between volcanic flows and fresh impact craters some local erosional surfaces are found. (c) Geological cross section to summarize stratigraphic relationships. The green dashed line is the upper surface of sedimentary rocks extrapolated from buttes and outcrops preserved after erosion.

7. Discussion

7.1. Formation of the Sedimentary Plain Unit

Intercrater plains, covering more than 250,000,000 km^2 of the studied area, are nearly horizontal, with a N-S average gradient of 1.1% over 300 km and a W-E average gradient of 0.8% over 400 km. They are characterized by light-toned layered rocks and carved by erosional windows and impact craters. Erosional windows do not show a particular spatial distribution and, in most cases, they are filled by Hesperian lava flows.

Planar-layered rocks, local cross-bedding stratification, the presence of boxwork-like features, and polygonal cracks characterize these light-toned layered rocks. All of these features, which imply various grain sizes and depositional environments (e.g., planar light-toned layered deposits imply less energetic and smaller grain sizes than cross-bedding stratification) and further diagenetic evolution, are consistent with a sedimentary origin. These observations may imply two different sediment grain sizes and consequently two different depositional environments, which could be either subaqueous or subaerial. In situ analyses are required to investigate their origin.

Planar-layered rocks, which are ubiquitous in the erosional windows of sedimentary plains, require a low-energy deposition, subaerial or subaqueous. However, uniform airfall mantling is not consistent with the geometry of the sedimentary unit for two reasons. First, its topographic distribution is very homogeneous, at elevations between +500 m and −2000 below the datum. If deposited by wind, there is no reason why these deposits would fill plains so flat. Loess deposits, which are the terrestrial equivalent, are known to be irregular in thickness and surface topography [*Kukla and An*, 1989]. Second, stratigraphic contacts between sedimentary rocks (green unit) and crustal outcrops (brown unit) systematically display onlaps, as in the example of Figure 15, with sediments embaying the ancient buttes. Aerial deposits would have draped the buttes while here the possibly weaker material on buttes is unrelated to the flat-lying layered rocks of the smooth

Table 3. Summary of Erosional Rates on Mars From Previous Works Compared to the Erosional Rate Estimated in Our Studied Area

Location	Estimated Time (Ga)	Average Erosion Rate (nm/yr)	Source
Craters (Sinus Sabaeus and Margaritifer Sinus regions)	3.95–3.7	800	*Craddock et al.* [1997]
Craters (Arsia Mons region)	3.95–3.7	1000	*Hartmann et al.* [1999]
Craters (equatorial regions)	3.95–3.0	1295	*Craddock and Maxwell* [1993]
Meridiani	3.83–3.7	7700	*Hynek and Phillips* [2001]
Craters (Noachian regions)	3.83–3.7	7700	*Carr* [1992]
Valles Marineris	3.7–3.0	>10,000	*Michalski and Niles* [2012]
Craters	3.7–0	18	*Carr* [1992]
Gusev (crater)	3.6–0	0.8	*Grant et al.* [2006b]
Gusev (crater)Gale (crater)	3.5–03.3/3.2–0	0.0310	*Golombek et al.* [2006]*Newsom et al.* [2015]
Crater	3.2–0	1	*Arvidson et al.* [1979]
Meridiani, landing site	3.1–0	0.02	*Golombek and Bridges* [2000]
Pedestal crater	3.0–0	100	*Arvidson et al.* [1979]
Meridiani	3.0–0	15	*Golombek et al.* [2006]
Meridiani	0.4–0	12.2	*Golombek et al.* [2006]
Meridiani	0.4–0	1.3	*Golombek et al.* [2006]
Kitty Clyde's Sister (crater)	0.02	0.55	*Golombek et al.* [2014]
Eagle (crater)	0.01–0.004	0.34	*Golombek et al.* [2006], *Grant et al.* [2006a, 2008], and *Golombek et al.* [2014]
Voskhod (crater)	0.01–0.004	0.34	*Golombek et al.* [2014]
Emma Dean (crater)	0.004–0.002	0.73	*Golombek et al.* [2014]
Santa Maria (crater)	0.002–0.0006	2.6	*Golombek et al.* [2014]
Kaikos (crater)	0.0006–0.0002	0.5	*Golombek et al.* [2010, 2014]
Nerius (crater)	0.0006–0.0002	0	*Golombek et al.* [2010, 2014]
Nautilus (crater)	0.0006–0.0002	0.5	*Golombek et al.* [2010, 2014]
Concepcion (crater)	~0.0001	10	*Golombek et al.* [2010, 2014]
Hellas rim (north-west)	**3.7–3.3**[a]	>**1000**[a]	This study

[a]Bold values indicate the results of this study.

plains. Moreover, this weaker material is not spatially homogeneous, covering only a few sides of the buttes, and the thickness is not constant. Shallow channels frequently carve it, corroborating its weak nature.

From these observations, i.e., the homogeneous elevation and the widespread planar stratigraphy, we interpret the sedimentary plains as being deposited in a lacustrine or palustrine setting (e.g., an alluvial plain). This does not exclude the possibility of an eolian contribution to any standing body of water, despite being a depositional mechanism more difficult to justify based on the topographic and geological appearance of the studied area. *Moore and Wilhelms* [2001, 2007], *Crown et al.* [2005], *Wilson et al.* [2007], and *Bernhardt et al.* [2016] hypothesized that in Hellas there would be extended periods of fluvial activity and that the Hellas rim could be the margin of the lake hosted inside the Hellas basin. We agree with these authors and point out that the northwestern rim of the Hellas basin has undergone major aqueous episode(s) and could be the margin of a much larger ancient lake or ocean. The presence of smectite is a possible indicator of the existence of a paleo-ocean. In fact, on Earth, smectite occurs in various paleogeographical settings from nearshore shelf to oceanic basin and generally corresponds to relatively low sedimentation rates. Smectite appears to be a diagnostic mineral of the oceanic environment [*Thiry and Jacquin*, 1993].

The example outcrop in Figure 9 contains 70 m thick cross-bedded strata; cross-stratified rocks arranged as sets of conformable curving strata that are separated from adjacent sets by erosional surfaces and channels with tangential edges. Cross-bedding stratification involves sand-like grain sizes, but with HiRISE, the resolution is not sufficient to determine the grain size to verify if inverse grading is present. Figure 9b displays an extensive erosional surface underlain by truncated "lenses" outlined by light blue arrows. These lenses are shaped like individual channel deposits in cross section (possible buried channels). Such channels would be 6 m in width and would indicate the presence of alluvial conditions (Figure 9). Although it is not possible to identify the source area of these cross-stratified rocks, we favor a fluvial origin for the overall cross-bedded sediments because of their internal architecture and stratigraphic relationships between the channels.

Sedimentary rocks are characterized by the local presence of boxwork-like features (Figure 8). On Earth, boxwork structures were first described in Wind Cave, South Dakota, U.S. [*Bakalowicz et al.*, 1987], while on Mars

they were more recently described in the Gale crater by *Siebach and Grotzinger* [2014]. The presence of boxwork-like features implies different postdepositional processes, such as sedimentation and lithification of the rock, subsequent fracturing of the latter, with final saturation by brine-enriched fluids permeated over the fractures and mineral precipitation in veins. Lastly, the veins were exhumed and the less-cemented host rock was more eroded, forming protruding veins now exposed as polygonal ridges. *Siebach and Grotzinger* [2014] explained that a large amount of water filling pores is required to form boxworks.

In our studied area, rectangular and polygonal cracks form perpendicular to outcrop surfaces and are shallow. This perpendicular relationship is maintained regardless of the slope angle and aspect (direction). Such cracks are absent on fresh cliff faces. Based on these characteristics, we interpret them to have formed by weathering. Such crack patterns are generally formed by expansion and contraction of the rock [*Eves*, 2005] or humidity retention along cracks leading to differential weathering [*Netoff*, 1971]. These cracks are frequent in Martian sediments but do not indicate specific depositional or diagenetic characteristics, apart from the fact that the sediments were significantly indurated [*El-Maarry et al*., 2015]. This cementation may be due to burial and fluid circulation, corroborating the hypothesis of the presence of a standing water table in this area. Smectitic clay signatures were found in planar light-toned layers exposed within erosional windows in the presence of cracks. Further experiments by *El-Maarry et al*. [2015] also suggest that limited smectite abundance is sufficient to induce cracking. Previous work indicates that this region may have hosted more regional groundwater distribution unrelated to the water involved in the deposition of the sediments [*Andrews-Hanna and Lewis*, 2011].

7.2. Implications for Noachian/Hesperian Climatic Conditions

Our geological study sheds light on the nature and timing of intercrater plains of the northwestern rim of the Hellas basin. Geomorphic and geological evidence reveals an extended history of widespread sedimentary deposition followed by fissural volcanism. The main difference with some of the previous works [*Tanaka*, 1986; *Leonard and Tanaka*, 2001; *Tanaka et al*., 2014] lies in the identification of many smooth plains as being sedimentary and not volcanic in nature. The age of the sedimentary rocks identified (>3.7 Ga, Late Noachian) is in agreement with the intense erosional period in the Late Noachian and Early Hesperian elsewhere on Mars [*Craddock and Howard*, 2002] including in the Hellas region [*Wilson et al*., 2007; *Ansan et al*., 2011] and coeval with the highland valley network (3.7 Ga [*Fassett and Head*, 2008; *Ansan and Mangold*, 2013]). Flood volcanism appears spatially restricted to relatively small areas and limited in time to the Hesperian period, at ~3.3 Gy. The age of these flows is consistent with an overall Hesperian volcanism period as evidenced in the Hesperia Planum and Tyrrhena Patera volcanic provinces east of the Hellas basin [*Williams et al*., 2010; *Ody et al*., 2012]. Based on mineralogical observations, phyllosilicates are found predominantly associated with the Noachian-aged light-toned layered terrains, supporting the idea that the early weathering environment on the planet was dominated by water-rock interactions [*Poulet et al*., 2005; *Bibring et al*., 2006; *Ody et al*., 2012; *Carter et al*., 2013a], whereas Hesperian lava flows do not seem to be aqueous-altered.

Further studies are needed to clarify the source of the thick sedimentary deposits. We deduced that these sedimentary rocks were formed in the same period (3.7 Ga, Late Noachian) or before the valley networks but no direct relationship (e.g., valleys carving sedimentary rocks) was observed. Nevertheless, the northern group of sedimentary units is surrounded by many valley networks (Figure 3a). All well-developed valley networks are present at elevations higher than the highest elevations of the sedimentary intercrater plains between −513 m and −779 m. The abrupt cessation of valley networks above a specific altitude (−779 m) might be explained by two factors: the presence of a water table or eolian deposition covering the whole mapped area. We strongly favor a water table control of the valley network base level because of the wide extent of the study area. In contrast, valleys at lower elevations are mostly late-stage poorly branched valleys, locally crossing type II craters and unrelated to the Late Noachian networks.

Erosional unconformities of different scales (local to global) are an ubiquitous element of the whole study area. Recognizing unconformities is useful for subdividing stratigraphic units, interpreting lateral facies relationships, correlating certain stratigraphic boundaries, and reconstructing paleogeography. We observed two large regional erosional surfaces, as shown in the stratigraphic column of Figure 19b. The older one is located between the crustal outcrops (Hellas shoulder) and sediments and dated to the Noachian. The younger regional erosional surface lies between sedimentary rocks and volcanic flows, whose age is

comprised between the Late Noachian and the Late Hesperian. Erosional surfaces in the Hesperian period have previously been observed on the Hellas basin shoulder, for example, between Hesperian-aged alluvial cones and older sediments under these cones [*Moore and Howard*, 2005; *Kraal et al*., 2008; *Ansan et al*., 2011; *Howard and Moore*, 2011; *Morgan et al*., 2014]. These may result from the proposed global climatic change that occurred after the Late Noachian [*Golombek et al*., 2014].

Although we estimated the amount of sediment that would have been eroded within the study area (e.g., about 350 m in height), we did not directly observe evidence of how the materials were eroded. For example, spectroscopic observations did not indicate chemical constituents (such as hydrated sulfate or salts) that would have suggested dissolution. Dissolution may be a process consistent with burial, cementation, and fluid circulation. However, no chemical sediments were identified from the mineralogical observations, although we cannot exclude that they were present and fully dissolved. Fluvial erosion is a possibility suggested by late-stage fluvial channels (Figure 3a), but they would not leave the topography with enclosed depressions. Given the presence of grooves and flutes in some of the erosional windows, wind is the more appropriate agent of erosion.

The erosion rate estimated in this work is >1000 nm/yr, which is the same as for the Late Noachian/Early Hesperian period estimated by previous authors (see Table 3), whereas *Michalski and Niles* [2012] estimated an erosion rate 10 times larger for the same period (>10,000 nm/yr locally in Valles Marineris). We report the different erosion rates on Mars in units of nm/yr in Table 3. Volcanic flows (3.29 Ga) do not display evidence of intense erosion and are well preserved. The limited erosion of Late Hesperian volcanic flows is consistent with the low Martian erosion rates estimated by *Arvidson et al*. [1979], *Carr* [1992], *Golombek et al*. [2006], and *Grant et al*. [2006a].

By comparison with Earth, the erosional rate calculated in our studied area (~1000 nm/yr) is only 10 times slower than the lowest denudation rates on Earth (10,000 to 100,000 nm/yr), which have been reported in wet or dry cratonic areas [*Judson and Ritter*, 1964; *Saunders and Young*, 1983; *Summerfield*, 2005] although measured as an average over 400 My. The Noachian era is characterized by denudation rates that are much faster (more than 2 orders of magnitude) than subsequent epochs and are similar to the erosion rates on Earth in continental areas that are dominated by liquid water [*Judson and Ritter*, 1964; *Saunders and Young*, 1983; *Portenga and Bierman*, 2011]. The limited Hesperian erosion compared to the Noachian erosion in the studied area corroborates the hypothesis proposed by *Golombek et al*. [2014], suggesting that the change in climate occurred after the Late Noachian on Mars.

8. Conclusion

Our new detailed geological map (1:25,000) of the intercrater plains north of the Hellas basin, achieved with data from Mars Express, Mars Reconnaissance Orbiter, and Mars Odyssey offers a new perspective for the geological history of this region. Our results refine the interpretation of the nature (volcanic and sedimentary) and age of intercrater plains. The northern part of the Hellas basin contains a topographically flat area, which was formed during the Late Noachian by sedimentary deposition and later, in the Late Hesperian, by effusive volcanism. Due to the large number of erosional windows within the region, we were able to investigate the morphology and mineralogy of the units to interpret their lithology. Light-toned materials characterize these units with frequent subhorizontal bedding over a broad extent (greater than tens of kilometers), with spectral identifications of Fe/Mg phyllosilicates, occasionally presenting localized cross-bedding stratification. We interpret these units as being sedimentary in nature. These sedimentary rocks, covering an area 7.5 times bigger (250,000,000 km^2) than that covered by volcanic flows, are probably related to aqueous deposition, which would explain their broad extent, flat topography, and cementation related to fluid circulation, although the latter characteristics might also be related to regional groundwater circulation [*Andrews-Hanna and Lewis*, 2011] of previously dry sediments (such as eolian sediments). These Noachian sediments are locally covered by dark-toned rough Hesperian pyroxene-bearing lava flows.

Moreover, the presence of an erosional surface between sediment deposits and lava flows, which is probably Late Noachian–Early Hesperian in age, implies an important erosional cycle during this period, for which we estimated a minimum erosional rate of >1000 nm/yr. Knowledge of the erosion and depositional cycle in time and space, erosional rate quantification, and the related water budget also adds to our understanding of the past Martian climate.

Acknowledgments

The authors wish to thank Sharon Wilson and two anonymous reviewers for their thorough and insightful reviews. The work reported here was supported by funding from the Italian Ministry of University and Research (MIUR). The authors wish to thank MRO/HiRISE and CRISM, as well as Mars Express/HRSC and OMEGA teams for images and DEMs. The data were obtained from the Planetary Data System (PDS) (https://pds.nasa.gov/index.shtml). CTX and HiRISE data were processed using ISIS (Integrated Software for Imagers and Spectrometers) (http://isis.astrogeology.usgs.gov) and AMES Stereo Pipeline (http://ti.arc.nasa.gov/tech/asr/intelligent-robotics/ngt/stereo/). The French authors were funded by the Centre National d'Etudes Spatial (CNES).

References

Andrews-Hanna, J. C., and K. W. Lewis (2011), Early Mars hydrology: 2. Hydrological evolution in the Noachian and Hesperian epochs, *J. Geophys. Res.*, *116*, E02007, doi:10.1029/2010JE003709.

Ansan, V., and N. Mangold (2013), 3D morphometry of valley networks on Mars from HRSC/MEX DEMs: Implications for climatic evolution through time, *J. Geophys. Res. Planets*, *118*, 1873–1894, doi:10.1002/jgre.20117.

Ansan, V., et al. (2011), Stratigraphy, mineralogy, and origin of layered deposits inside Terby crater, Mars, *Icarus*, *211*(1), 273–304, doi:10.1016/J.Icarus.2010.09.011.

Arvidson, R., E. Guinness, and S. Lee (1979), Differential aeolian redistribution rates on Mars, *Nature*, *278*, 533–535.

Bakalowicz, M. J., D. C. Ford, T. E. Miller, A. N. Palmer, and M. V. Palmer (1987), Thermal genesis of dissolution caves in the Black Hills, South Dakota, *Geol. Soc. Am. Bull.*, *99*(6), 729–738.

Bandfield, J. L. (2002), Global mineral distributions on Mars, *J. Geophys. Res.*, *107*(E6), 5042, doi:10.1029/2001JE001510.

Bandfield, J. L., and M. D. Smith (2003), Multiple emission angle surface–atmosphere separations of Thermal Emission Spectrometer data, *Icarus*, *161*(1), 47–65.

Bandfield, J. L., V. E. Hamilton, and P. R. Christensen (2000), A global view of Martian surface compositions from MGS-TES, *Science*, *287*(5458), 1626–1630.

Bernhardt, H., H. Hiesinger, M. A. Ivanov, O. Ruesch, G. Erkeling, and D. Reiss (2016), Photogeologic mapping and the geologic history of the Hellas basin floor, Mars, *Icarus*, *264*, 407–442.

Bibring, J. P., A. Soufflot, M. Berthé, Y. Langevin, B. Gondet, P. Drossart, M. Bouyé, M. Combes, P. Puget, and A. Semery (2004), OMEGA: Observatoire pour la Minéralogie, l'Eau, les Glaces et l'Activité, paper presented at Mars Express: The Scientific Payload.

Bibring, J. P., et al. (2006), Global mineralogical and aqueous Mars history derived from OMEGA/Mars Express data, *Science*, *312*(5772), 400–404, doi:10.1126/science.1122659.

Bishop, J. L., M. Parente, C. M. Weitz, E. Z. Noe Dobrea, L. H. Roach, S. L. Murchie, P. C. McGuire, N. K. McKeown, C. M. Rossi, and A. J. Brown (2009), Mineralogy of Juventae Chasma: Sulfates in the light-toned mounds, mafic minerals in the bedrock, and hydrated silica and hydroxylated ferric sulfate on the plateau, *J. Geophys. Res.*, *114*, E00D09, doi:10.1029/2009JE003352.

Broxton, M. J., and L. J. Edwards (2008), The Ames Stereo Pipeline: Automated 3D surface reconstruction from orbital imagery, *Lunar Planet. Sci.*, *XXXIX*, *Abstract 2419*.

Carr, M. H. (1992), Post-Noachian erosion rates: Implications for Mars climate change, *Lunar Planet. Sci.*, *XXIII*, *205–206*.

Carter, J., F. Poulet, N. Mangold, V. Ansan, and D. Loizeau (2011), Mineralogical evidence for major aqueous activity in the northern Hellas province, Mars, paper presented at EPSC/DPS.

Carter, J., F. Poulet, J. P. Bibring, N. Mangold, and S. Murchie (2013a), Hydrous minerals on Mars as seen by the CRISM and OMEGA imaging spectrometers: Updated global view, *J. Geophys. Res. Planets*, *118*, 831–858, doi:10.1029/2012JE004145.

Carter, J., F. Poulet, S. Murchie, and J. P. Bibring (2013b), Automated processing of planetary hyperspectral datasets for the extraction of weak mineral signatures and applications to CRISM observations of hydrated silicates on Mars, *Planet. Space Sci.*, *76*, 53–67.

Christensen, P. R., D. L. Anderson, S. C. Chase, R. T. Clancy, R. N. Clark, B. J. Conrath, H. H. Kieffer, R. O. Kuzmin, M. C. Malin, and J. C. Pearl (1998), Results from the Mars Global Surveyor Thermal Emission Spectrometer, *Science*, *279*(5357), 1692–1698.

Christensen, P. R., J. L. Bandfield, J. F. Bell III, N. Gorelick, V. E. Hamilton, A. Ivanov, B. M. Jakosky, H. H. Kieffer, M. D. Lane, and M. C. Malin (2003), Morphology and composition of the surface of Mars: Mars Odyssey THEMIS results, *Science*, *300*(5628), 2056–2061.

Christensen, P. R., B. M. Jakosky, H. H. Kieffer, M. C. Malin, H. Y. McSween Jr., K. Nealson, G. L. Mehall, S. H. Silverman, S. Ferry, and M. Caplinger (2004), The Thermal Emission Imaging System (THEMIS) for the Mars 2001 Odyssey mission, *Space Sci. Rev.*, *110*(1-2), 85–130.

Craddock, R. A., and A. D. Howard (2002), The case for rainfall on a warm, wet early Mars, *J. Geophys. Res.*, *107*(E11), 5111, doi:10.1029/2001JE001505.

Craddock, R. A., and T. A. Maxwell (1993), Geomorphic evolution of the Martian highlands through ancient fluvial processes, *J. Geophys. Res.*, *98*(E2), 3453–3468, doi:10.1029/92JE02508.

Craddock, R. A., T. A. Maxwell, and A. D. Howard (1997), Crater morphometry and modification in the Sinus Sabaeus and Margaritifer Sinus regions of Mars, *J. Geophys. Res.*, *102*(E6), 13,321–13,340, doi:10.1029/97JE01084.

Crown, D. A., L. F. Bleamaster, and S. C. Mest (2005), Styles and timing of volatile-driven activity in the eastern Hellas region of Mars, *J. Geophys. Res.*, *110*, E12S22, doi:10.1029/2005JE002496.

De Hon, R. A. (1992), Martian lake basins and lacustrine plains, *Earth Moon Planets*, *56*(2), 95–122.

Di Achille, G., and B. M. Hynek (2010), Ancient ocean on Mars supported by global distribution of deltas and valleys, *Nat. Geosci.*, *3*(7), 459–463.

Edgett, K. S., and M. C. Malin (2002), Martian sedimentary rock stratigraphy: Outcrops and interbedded craters of northwest Sinus Meridiani and southwest Arabia Terra, *Geophys. Res. Lett.*, *29*(24), 2179, doi:10.1029/2002GL016515.

Edwards, C. S., J. L. Bandfield, P. R. Christensen, and A. D. Rogers (2014), The formation of infilled craters on Mars: Evidence for widespread impact induced decompression of the early Martian mantle? *Icarus*, *228*, 149–166.

Ehlmann, B. L., et al. (2008), Orbital identification of carbonate-bearing rocks on Mars, *Science*, *322*(5909), 1828–1832, doi:10.1126/science.1164759.

El-Maarry, M. R., W. Watters, N. K. McKeown, J. Carter, E. N. Dobrea, J. L. Bishop, A. Pommerol, and N. Thomas (2014), Potential desiccation cracks on Mars: A synthesis from modeling, analogue-field studies, and global observations, *Icarus*, *241*, 248–268.

El-Maarry, M. R., A. Pommerol, and N. Thomas (2015), Desiccation of phyllosilicate-bearing samples as analog for desiccation cracks on Mars: Experimental setup and initial results, *Planet. Space Sci.*, *111*, 134–143.

Eves, R. L. (2005), *Water, Rock, & Time: The Geologic Story of Zion National Park*, Zion Natural History Association, Utah.

Fassett, C. I., and J. W. Head (2008), The timing of Martian valley network activity: Constraints from buffered crater counting, *Icarus*, *195*(1), 61–89, doi:10.1016/J.Icarus.2007.12.009.

Golombek, M. P., and N. T. Bridges (2000), Erosion rates on Mars and implications for climate change: Constraints from the Pathfinder landing site, *J. Geophys. Res.*, *105*(E1), 1841–1853, doi:10.1029/1999JE001043.

Golombek, M. P., J. A. Grant, L. S. Crumpler, R. Greeley, R. E. Arvidson, J. F. Bell, C. M. Weitz, R. Sullivan, P. R. Christensen, and L. A. Soderblom (2006), Erosion rates at the Mars Exploration Rover landing sites and long-term climate change on Mars, *J. Geophys. Res.*, *111*, E12S10, doi:10.1029/2006JE00275.

Golombek, M. P., K. Robinson, A. S. McEwen, N. T. Bridges, B. A. Ivanov, L. Tornabene, and R. Sullivan (2010), Constraints on ripple migration at Meridiani Planum from Opportunity and HiRISE observations of fresh craters, *J. Geophys. Res.*, *115*, E00F08, doi:10.1029/2010JE003628.

Golombek, M. P., N. H. Warner, V. Ganti, M. P. Lamb, T. J. Parker, R. L. Fergason, and R. Sullivan (2014), Small crater modification on Meridiani Planum and implications for erosion rates and climate change on Mars, *J. Geophys. Res. Planets*, *119*, 2522–2547, doi:10.1002/2014JE004658.

Grant, J. A., R. E. Arvidson, L. S. Crumpler, M. P. Golombek, B. Hahn, A. F. C. Haldemann, R. Li, L. A. Soderblom, S. W. Squyres, and S. P. Wright (2006a), Crater gradation in Gusev crater and Meridiani Planum, Mars, *J. Geophys. Res.*, *111*, E02S08, doi:10.1029/2005JE002465.

Grant, J. A., S. A. Wilson, S. W. Ruff, M. P. Golombek, and D. L. Koestler (2006b), Distribution of rocks on the Gusev Plains and on Husband Hill, Mars, *Geophys. Res. Lett.*, *33*, L16202, doi:10.1029/2006GL026964.

Grant, J. A., S. A. Wilson, B. A. Cohen, M. P. Golombek, P. E. Geissler, R. J. Sullivan, R. L. Kirk, and T. J. Parker (2008), Degradation of Victoria crater, Mars, *J. Geophys. Res.*, *113*, E11010, doi:10.1029/2008JE003155.

Greeley, R., and J. Guest (1987), Geologic map of the eastern equatorial region of Mars, The Survey.

Greeley, R., and P. D. Spudis (1981), Volcanism on Mars, *Rev. Geophys.*, *19*(1), 13–41, doi:10.1029/RG019i001p00013.

Hamilton, V. E., and P. R. Christensen (2005), Evidence for extensive, olivine-rich bedrock on Mars, *Geology*, *33*(6), 433–436.

Hartmann, W. K. (2005), Martian cratering 8: Isochron refinement and the chronology of Mars, *Icarus*, *174*(2), 294–320.

Hartmann, W. K., and G. Neukum (2001), Cratering chronology and the evolution of Mars, in *Chronology and Evolution of Mars*, edited by R. Kallenbach, J. Geiss, and W. K. Hartmann, pp. 165–194, Springer, Netherlands.

Hartmann, W. K., M. C. Malin, A. S. McEwen, M. H. Carr, L. A. Soderblom, P. Thomas, E. Danielson, P. James, and J. Veverka (1999), Evidence for recent volcanism on Mars from crater counts, *Nature*, *397*(6720), 586–589.

Hoefen, T. M., R. N. Clark, J. L. Bandfield, M. D. Smith, J. C. Pearl, and P. R. Christensen (2003), Discovery of olivine in the Nili Fossae region of Mars, *Science*, *302*(5645), 627–630.

Hon, K., J. Kauahikaua, R. Denlinger, and K. Mackay (1994), Emplacement and inflation of pahoehoe sheet flows: Observations and measurements of active lava flows on Kilauea Volcano, Hawaii, *Geol. Soc. Am. Bull.*, *106*(3), 351–370.

Howard, A. D., and J. M. Moore (2011), Late Hesperian to early Amazonian midlatitude Martian valleys: Evidence from Newton and Gorgonum basins, *J. Geophys. Res.*, *116*, E05003, doi:10.1029/2010JE003782.

Hynek, B. M., and R. J. Phillips (2001), Evidence for extensive denudation of the Martian highlands, *Geology*, *29*(5), 407–410, doi:10.1130/0091-7613(2001)029<0407:Efedot>2.0.Co;2.

Ivanov, B. A. (2001), Mars/Moon cratering rate ratio estimates, in *Chronology and Evolution of Mars*, edited by R. Kallenbach, J. Geiss, and W. K. Hartmann, pp. 87–104, Springer, Netherlands.

Jaumann, R., G. Neukum, T. Behnke, T. C. Duxbury, K. Eichentopf, J. Flohrer, S. V. Gasselt, B. Giese, K. Gwinner, and E. Hauber (2007), The high-resolution stereo camera (HRSC) experiment on Mars Express: Instrument aspects and experiment conduct from interplanetary cruise through the nominal mission, *Planet. Space Sci.*, *55*(7), 928–952.

Judson, S., and D. F. Ritter (1964), Rates of regional denudation in the United States, *J. Geophys. Res.*, *69*(16), 3395–3401, doi:10.1029/JZ069i016p03395.

Kneissl, T., S. van Gasselt, and G. Neukum (2011), Map-projection-independent crater size-frequency determination in GIS environments—New software tool for ArcGIS, *Planet. Space Sci.*, *59*(11), 1243–1254.

Kraal, E. R., E. Asphaug, J. M. Moore, A. Howard, and A. Bredt (2008), Catalogue of large alluvial fans in Martian impact craters, *Icarus*, *194*(1), 101–110.

Kukla, G., and Z. An (1989), Loess stratigraphy in central China, *Palaeogeogr. Palaeoclimatol. Palaeoecol.*, *72*, 203–225.

Leake, M. A. (1982), The intercrater plains of Mercury and the Moon: Their nature, origin, and role in terrestrial planet evolution, Tech. Memo. 84894, pp. 3–535, NASA, Washington, D. C.

Leonard, G. J., and K. L. Tanaka (2001), Geologic map of the Hellas region of Mars, U.S. Department of the Interior, U.S. Geological Survey.

Loizeau, D., J. Carter, S. Bouley, N. Mangold, F. Poulet, J. P. Bibring, F. Costard, Y. Langevin, B. Gondet, and S. L. Murchie (2012), Characterization of hydrated silicate-bearing outcrops in Tyrrhena Terra, Mars: Implications to the alteration history of Mars, *Icarus*, *219*(1), 476–497.

Malin, M. C. (1976), Nature and origin of intercrater plains on Mars, *Stud. Martian Geol.*, 101–176.

Malin, M. C., and D. Dzurisin (1977), Landform degradation on Mercury, the Moon, and Mars: Evidence from crater depth/diameter relationships, *J. Geophys. Res.*, *82*(2), 376–388, doi:10.1029/JB082i002p00376.

Malin, M. C., et al. (2007), Context camera investigation on board the Mars Reconnaissance Orbiter, *J. Geophys. Res.*, *112*, E05S04, doi:10.1029/2006JE002808.

Mangold, N., and V. Ansan (2006), Detailed study of an hydrological system of valleys, a delta and lakes in the Southwest Thaumasia region, Mars, *Icarus*, *180*(1), 75–87, doi:10.1016/J.Icarus.2005.08.017.

Mangold, N., S. Adeli, S. Conway, V. Ansan, and B. Langlais (2012), A chronology of early Mars climatic evolution from impact crater degradation, *J. Geophys. Res.*, *117*, E04003, doi:10.1029/2011JE004005.

McEwen, A. S., et al. (2007), Mars Reconnaissance Orbiter's High Resolution Imaging Science Experiment (HiRISE), *J. Geophys. Res.*, *112*, E05S02, doi:10.1029/2005JE002605.

Metz, J. M., J. P. Grotzinger, D. Mohrig, R. E. Milliken, B. Prather, C. Pirmez, A. S. McEwen, and C. M. Weitz (2009), Sublacustrine depositional fans in southwest Melas Chasma, *J. Geophys. Res.*, *114*, E10002, doi:10.1029/2009JE003365.

Michael, G. G. (2013), Planetary surface dating from crater size–frequency distribution measurements: Multiple resurfacing episodes and differential isochron fitting, *Icarus*, *226*(1), 885–890.

Michael, G. G., and G. Neukum (2010), Planetary surface dating from crater size–frequency distribution measurements: Partial resurfacing events and statistical age uncertainty, *Earth Planet. Sci. Lett.*, *294*(3), 223–229.

Michael, G. G., T. Platz, T. Kneissl, and N. Schmedemann (2012), Planetary surface dating from crater size–frequency distribution measurements: Spatial randomness and clustering, *Icarus*, *218*(1), 169–177.

Michalski, J. R., and P. B. Niles (2012), Atmospheric origin of Martian interior layered deposits: Links to climate change and the global sulfur cycle, *Geology*, *40*(5), 419–422.

Michalski, J. R., and C. L. Smith (2015), Clay minerals on Mars: Updated crystal-chemistry from infrared remote sensing and comparison to meteorite data, *LPI Contributions*, *1856*, 5097.

Milliken, R. E., J. F. Mustard, F. Poulet, D. Jouglet, J. P. Bibring, B. Gondet, and Y. Langevin (2007), Hydration state of the Martian surface as seen by Mars Express OMEGA: 2. H_2O content of the surface, *J. Geophys. Res.*, *112*, E08S07, doi:10.1029/2006JE00285.

Moore, J. M., and A. D. Howard (2005), Large alluvial fans on Mars, *J. Geophys. Res.*, *110*, E04005, doi:10.1029/2004JE002352.

Moore, J. M., and D. E. Wilhelms (2001), Hellas as a possible site of ancient ice-covered lakes on Mars, *Icarus*, *154*(2), 258–276.

Moore, J. M., and D. E. Wilhelms (2007), Geologic map of part of the Western Hellas Planitia, Mars, Geological Survey (US).

Moratto, Z. M., M. J. Broxton, R. A. Beyer, M. Lundy, and K. Husmann (2010), Ames Stereo Pipeline, NASA's open source automated stereogrammetry software, *Lunar Planet. Sci., XLI, Abstract 2364*.

Morgan, A. M., A. D. Howard, D. E. J. Hobley, J. M. Moore, W. E. Dietrich, R. M. E. Williams, D. M. Burr, J. A. Grant, S. A. Wilson, and Y. Matsubara (2014), Sedimentology and climatic environment of alluvial fans in the Martian Saheki crater and a comparison with terrestrial fans in the Atacama Desert, *Icarus*, *229*, 131–156.

Murchie, S. L., et al. (2007), Compact reconnaissance imaging spectrometer for Mars (CRISM) on Mars reconnaissance orbiter (MRO), *J. Geophys. Res.*, *112*, E05S03, doi:10.1029/2006JE002682.

Mustard, J. F., S. L. Murchie, S. M. Pelkey, B. L. Ehlmann, R. E. Milliken, J. A. Grant, J. P. Bibring, F. Poulet, J. L. Bishop, and E. N. Dobrea (2008), Hydrated silicate minerals on Mars observed by the Mars Reconnaissance Orbiter CRISM instrument, *Nature*, *454*(7202), 305–309.

Netoff, D. I. (1971), Polygonal jointing in sandstone near Boulder, Colorado, *Mt. Geol.*, *8*, 17–24.

Neukum, G., and R. Jaumann (2004), HRSC: The high resolution stereo camera of Mars Express, in *Mars Express: The Scientific Payload*, *Eur. Space Agency Spec. Publ*, ESA-SP, vol. 1240, edited by A. Wilson, pp. 17–35.

Newsom, H. E., N. Mangold, L. C. Kah, J. M. Williams, R. E. Arvidson, N. Stein, A. M. Ollila, J. C. Bridges, S. P. Schwenzer, and P. L. King (2015), Gale crater and impact processes—Curiosity's first 364 Sols on Mars, *Icarus*, *249*, 108–128.

Ody, A., F. Poulet, Y. Langevin, J. P. Bibring, G. Bellucci, F. Altieri, B. Gondet, M. Vincendon, J. Carter, and N. Manaud (2012), Global maps of anhydrous minerals at the surface of Mars from OMEGA/MEx, *J. Geophys. Res.*, *117*, E00J14, doi:10.1029/2012JE004117.

Ody, A., F. Poulet, J. P. Bibring, D. Loizeau, J. Carter, B. Gondet, and Y. Langevin (2013), Global investigation of olivine on Mars: Insights into crust and mantle compositions, *J. Geophys. Res. Planets*, *118*, 234–262, doi:10.1029/2012JE004149.

Ori, G. G., L. Marinangeli, and A. Baliva (2000), Terraces and Gilbert-type deltas in crater lakes in Ismenius Lacus and Memnonia (Mars), *J. Geophys. Res.*, *105*(E7), 17,629–17,641, doi:10.1029/1999JE001219.

Pondrelli, M., A. P. Rossi, L. Marinangeli, E. Hauber, K. Gwinner, A. Baliva, and S. Di Lorenzo (2008), Evolution and depositional environments of the Eberswalde fan delta, Mars, *Icarus*, *197*(2), 429–451.

Portenga, E. W., and P. R. Bierman (2011), Understanding Earth's eroding surface with 10 Be, *GSA Today*, *21*(8), 4–10.

Potter, D. B. (1976), Geologic map of the Hellas quadrangle of Mars, *U.S. Geol. Surv. Misc. Invest. Ser. Map I-941*, *scale 1:5,000,000*.

Poulet, F., et al. (2005), Phyllosilicates on Mars and implications for early Martian climate, *Nature*, *438*(7068), 623–627, doi:10.1038/nature04274.

Poulet, F., C. Gomez, J. P. Bibring, Y. Langevin, B. Gondet, P. Pinet, G. Belluci, and J. F. Mustard (2007), Martian surface mineralogy from Observatoire pour la Minéralogie, l'Eau, les Glaces et l'Activité on board the Mars Express spacecraft (OMEGA/MEx): Global mineral maps, *J. Geophys. Res.*, *112*, E08S02, doi:10.1029/2006JE002840.

Poulet, F., J. P. Bibring, Y. Langevin, J. F. Mustard, N. Mangold, M. Vincendon, B. Gondet, P. Pinet, J. M. Bardintzeff, and B. Platevoet (2009a), Quantitative compositional analysis of Martian mafic regions using the MEx/OMEGA reflectance data 1. Methodology, uncertainties and examples of application, *Icarus*, *201*(1), 69–83.

Poulet, F., N. Mangold, B. Platevoet, J. M. Bardintzeff, V. Sautter, J. F. Mustard, J. P. Bibring, P. Pinet, Y. Langevin, and B. Gondet (2009b), Quantitative compositional analysis of Martian mafic regions using the MEx/OMEGA reflectance data: 2. Petrological implications, *Icarus*, *201*(1), 84–101.

Rogers, A. D., and R. L. Fergason (2011), Regional-scale stratigraphy of surface units in Tyrrhena and Iapygia Terrae, Mars: Insights into highland crustal evolution and alteration history, *J. Geophys. Res.*, *116*, E08005, doi:10.1029/2010JE003772.

Rogers, A. D., and A. H. Nazarian (2013), Evidence for Noachian flood volcanism in Noachis Terra, Mars, and the possible role of Hellas impact basin tectonics, *J. Geophys. Res. Planets*, *118*, 1094–1113, doi:10.1002/jgre.20083.

Rogers, A. D., O. Aharonson, and J. L. Bandfield (2009), Geologic context of in situ rocky exposures in Mare Serpentis, Mars: Implications for crust and regolith evolution in the cratered highlands, *Icarus*, *200*(2), 446–462.

Saunders, I., and A. Young (1983), Rates of surface processes on slopes, slope retreat and denudation, *Earth Surf. Processes Landforms*, *8*(5), 473–501.

Scott, D. H., and M. H. Carr (1978), Geologic map of Mars, *U.S. Geol. Surv.*, *Map I-1083*.

Siebach, K. L., and J. P. Grotzinger (2014), Volumetric estimates of ancient water on Mount Sharp based on boxwork deposits, Gale Crater, Mars, *J. Geophys. Res. Planets*, *119*, 189–198, doi:10.1002/2013JE004508.

Smith, D. E., et al. (1999), The global topography of Mars and implications for surface evolution, *Science*, *284*(5419), 1495–1503.

Summerfield, M. A. (2005), A tale of two scales, or the two geomorphologies, *Trans. Inst. British Geogr.*, *30*(4), 402–415.

Tanaka, K. L. (1986), The stratigraphy of Mars, *J. Geophys. Res.*, *91*(B13), E139–E158, doi:10.1029/JB091ib13p0e139.

Tanaka, K. L., and P. A. Davis (1988), Tectonic history of the Syria Planum province of Mars, *J. Geophys. Res.*, *93*(B12), 14,893–14,917, doi:10.1029/JB093ib12p14893.

Tanaka, K. L., and G. J. Leonard (1995), Geology and landscape evolution of the Hellas region of Mars, *J. Geophys. Res.*, *100*(E3), 5407–5432, doi:10.1029/94JE02804.

Tanaka, K. L., S. J. Robbins, C. M. Fortezzo, J. A. Skinner, and T. M. Hare (2014), The digital global geologic map of Mars: Chronostratigraphic ages, topographic and crater morphologic characteristics, and updated resurfacing history, *Planet. Space Sci.*, *95*, 11–24, doi:10.1016/J.Pss.2013.03.006.

Thiry, M., and T. Jacquin (1993), Clay mineral distribution related to rift activity, sea-level changes and paleoceanography in the Cretaceous of the Atlantic Ocean, *Clay Miner.*, *28*, 61–61.

Werner, S. C. (2008), The early Martian evolution—Constraints from basin formation ages, *Icarus*, *195*(1), 45–60.

Whittow, J. B. (1984), *The Penguin Dictionary of Physical Geography*, Penguin books Hamondsworth, New York.

Wilhelms, D. E. (1974), Comparison of Martian and lunar geologic provinces, *J. Geophys. Res.*, *79*(26), 3933–3941, doi:10.1029/JB079i026p03933.

Williams, D. A., R. Greeley, R. L. Fergason, R. Kuzmin, T. B. McCord, J. P. Combe, J. W. Head, L. Xiao, L. Manfredi, and F. Poulet (2009), The circum-Hellas volcanic province, Mars: Overview, *Planet. Space Sci.*, *57*(8), 895–916.

Williams, D. A., R. Greeley, L. Manfredi, J. Raitala, G. Neukum, and H. C.-I. Team (2010), The circum-Hellas volcanic province, Mars: Assessment of wrinkle-ridged plains, *Earth Planet. Sci. Lett.*, *294*(3), 492–505.

Wilson, S. A., A. D. Howard, J. M. Moore, and J. A. Grant (2007), Geomorphic and stratigraphic analysis of Crater Terby and layered deposits north of Hellas basin, Mars, *J. Geophys. Res.*, *112*, E08009, doi:10.1029/2006JE002830.